Inferred basal friction and mass flux affected by crystal-orientation fabrics

Nicholas M. Rathmann ⓘ and David A. Lilien ⓘ

Niels Bohr Institute, University of Copenhagen, Copenhagen, Denmark

We investigate the errors caused by neglecting the crystal-orientation fabric when inferring the basal friction coefficient field, and whether such errors can be alleviated by inferring an isotropic enhancement factor field to compensate for missing fabric information. We calculate the steady states that arise from ice flowing over a sticky spot and a bedrock bump using a vertical-slab numerical ice-flow model, consisting of a Weertman sliding law and the anisotropic Johnson flow law, coupled to a spectral fabric model of lattice rotation and dynamic recrystallisation. Given the steady or transient states as input for a canonical adjoint-based inversion, we find that Glen's isotropic flow law cannot necessarily be used to infer the true basal drag or friction coefficient field, which are obscured by the orientation fabric, thus potentially affecting vertically integrated mass fluxes. By inverting for an equivalent isotropic enhancement factor, a more accurate mass flux can be recovered, suggesting that joint inversions for basal friction and the isotropic flow-rate factor may be able to compensate for mechanical anisotropies caused by the fabric. Thus, in addition to other sources of rheological uncertainty, fabric might complicate attempts to relate subglacial conditions to basal properties inferred from an inversion relying on Glen's law.

Introduction

Basal drag provides an important resistive component in the force budget of glaciers and ice sheets, with implications for the accuracy of mass-loss projections and the dynamics of ice streams (Echelmeyer and others, 1994; Gillet-Chaulet and others, 2012; Larour and others, 2012; Morlighem and others, 2013; Schoof and Mantelli, 2021). Basal drag is classically represented in the form of a sliding law following Weertman (1957), which relates the ice–bed sliding velocity to the resulting basal drag (synonymous with basal shear stress or basal traction) through a power law with an unknown friction coefficient and exponent. Using inverse methods that rely on surface-velocity and ice-thickness observations to infer the basal friction coefficient, large spatio-temporal variations in the friction coefficient, or corresponding basal drag, have previously been inferred over ice streams in Greenland and Antarctica (e.g. Joughin and others, 2004; Sergienko and others, 2014; Ranganathan and others, 2020; Maier and others, 2021).

Although ice streams flow primarily by sliding, complex basal conditions near their onset regions can lead to flow by a combination of sliding and internal deformation. Basal conditions near the onset of the largest ice stream in Greenland, the Northeast Greenland Ice Stream (NEGIS), have been extensively studied (Fahnestock and others, 2001; Christianson and others, 2014; Keisling and others, 2014; Beyer and others, 2018; Franke and others, 2021). NEGIS is notoriously challenging to reproduce in ice-flow models (Greve and Herzfeld, 2013; Rückamp and others, 2019), and its warm basal environment is likely central to its existence (Fahnestock and others, 2001; Smith-Johnsen and others, 2020). In the upstream part of NEGIS, active-source seismics and radio-echo sounding indicate the ice rests on water-saturated till, with a strong connection to the subglacial water system of its onset, and might be controlled by variations in basal friction further downstream (Christianson and others, 2014; Keisling and others, 2014; Franke and others, 2021). In general, the basal conditions of NEGIS are rather intricate, with areas of fast flow over a rough bed downstream of smoother-bedded areas near the onset (Franke and others, 2021). Similarly, the Ross ice streams of west Antarctic are the frequent subject of research attempting to understand the balance between driving stresses, basal drag, and lateral (shear-margin) drag in ice streams. It is believed that these ice streams are enabled by weak subglacial sediment, and that the relatively small driving stresses experienced (small slopes) are balanced by significant components of both lateral and basal drag (MacAyeal and others, 1995; Whillans and van der Veen, 1997; Hermann and Barclay, 1998; Kamb, 2001). The relatively smooth bed and direct evidence of subglacial sediment suggest that the Ross ice streams are likely areas where friction, rather than bedrock topography, is the primary cause of sticky spots (localised increased drag). Although early studies suggested that bedrock highs are the most likely cause of sticky spots beneath these ice streams (e.g. Alley, 1993), more recent work has focused on the connection to till strength and water availability (Anandakrishnan and Alley, 1997; Tulaczyk and others, 2000).

Variations in basal drag are generally thought to be the result of variations in the subglacial water pressure, temperature at the ice–bed interface, and composition and roughness of the bed. Inversion procedures for basal properties are, however, sensitive to rheological

cambridge.org/jog

uncertainties (e.g. Arthern and others, 2015); missing or approximated ice physics, as well as measurement error, can manifest itself in the inferred basal friction coefficient field. Nevertheless, inferring basal conditions by inversion is a prerequisite for modelling the transient flow of ice masses (e.g. DeConto and Pollard, 2016), which cannot reproduce surface-velocity observations without such calibration.

Strong anisotropic crystal orientation fabrics are common in deep layers of ice sheets (see review in Faria and others, 2014a) and are known to introduce mechanical anisotropies (Duval and others, 1983; Shoji and Langway, 1985, 1988). Numerical ice-flow modelling has shown that fabric anisotropies can affect the deformation of ice masses at large scales (Thorsteinsson and others, 2003; Gillet-Chaulet and others, 2006; Pettit and others, 2007; Martín and Gudmundsson, 2012; Hruby and others, 2020). Neglecting the orientation fabric by assuming isotropic ice (Glen's flow law) might therefore lead to an incorrect basal friction field being inferred, even if the isotropic flow-rate factor, A, is jointly inferred to compensate for rheological uncertainties due to missing fabric information. If so, this has two immediate implications. First, errors in the basal friction field affect the sliding velocity and thus the vertically integrated mass flux. Simulations of the kind undertaken for mass-loss projections use present conditions to infer the basal drag as calibration for transient simulations, and errors in the basal friction field may therefore bias mass-loss projections (depending on flow regime and flow approximations). Second, attempts to relate inferred spatio-temporal variations in the friction coefficient or basal drag fields to specific subglacial conditions and processes might be obscured by the orientation fabric.

In this study, we investigate the effect of approximating ice as isotropic when inferring the basal friction coefficient field over a subglacial sticky spot and bedrock bump using the canonical method of an adjoint-based inversion. Specifically, we consider flow regimes where *both* basal sliding and internal deformation are non-negligible, arguably relevant near ice-stream onsets and less so for fast sliding systems (e.g. outlet regions). For this purpose, we rely on a vertical slab anisotropic ice-flow model with a Weertman sliding law and a spectral fabric model, paired with an isotropic version of the same model, to isolate the effects of fabric anisotropy on inferred subglacial conditions. We subsequently investigate whether the concerns raised over neglecting the orientation fabric can be alleviated by accounting for an equivalent isotropic enhancement factor field.

Notation

Throughout the paper, primes shall be used to denote monocrystal rheological parameters and stresses/strain rates, as opposed to non-primed variables used to denote bulk (polycrystalline) rheological parameters and stresses/strain rates. Boldface symbols denote vectors or tensors, the order of the latter being implicit by the context. Let $\mathbf{a}$ and $\mathbf{b}$ be vectors, and $\mathbf{A}$ and $\mathbf{B}$ be second-order tensors. The following products are then used: $\mathbf{a} \cdot \mathbf{b} = a_i b_i$, $\mathbf{a}\mathbf{b} = a_i b_j$ (the outer, dyadic product), $\mathbf{A} \cdot \mathbf{a} = A_{ij} a_j$, $\mathbf{A} \cdot\!\cdot\, \mathbf{a}\mathbf{b} = A_{ij} a_j b_i$, $\mathbf{A} \cdot \mathbf{B} = A_{ij} B_{jk}$, and $\mathbf{A} \cdot\!\cdot\, \mathbf{B} = A_{ij} B_{ji} = \mathrm{tr}(\mathbf{A} \cdot \mathbf{B})$, where summation over repeated indices is implied. The identity matrix is denoted by $\mathbf{I}$, and the superscript T denotes the matrix transpose.

Anisotropic ice-flow modelling

We seek to separate the effect of fabric anisotropy from other sources of rheological uncertainty when inverting for the basal friction coefficient field using Glen's isotropic flow law. For this purpose, we perform a set of adjoint-based inversions (using Glen's law) of steady and transient states produced by an anisotropic flow law, and compare the results to the true friction coefficient field. As a frame of comparison (control) to weigh the Glen's law inversions against, we additionally carry out identical inversions using the anisotropic flow law itself. Doing so requires an anisotropic flow law that is simple enough for the inversion procedure to be feasible, yet can adequately reproduce (most) known effects that fabric anisotropy has on the directional viscosity structure of glacier ice. We find that Johnson's flow law fulfils both needs; it represents the lowest-order anisotropic extension of Glen's law at the expense of additionally accounting for a fabric-orientation vector field ($\mathbf{m}$) and two directional enhancement-factor fields (E_{mt} and E_{mm}). We therefore begin by introducing Johnson's law and the underlying fabric model used to determine $\mathbf{m}$, E_{mt}, and E_{mm}, which relies on a mixed Taylor–Sachs grain rheology. For the reader who is not interested in the technicalities of anisotropic ice-flow modelling, it is possible to skip to 'Numerical experiments', noting only the meaning of $\mathbf{m}$, E_{mt}, and E_{mm}.

Johnson's flow law

The dominant effect of fabric anisotropy on ice flow can be modelled using the transversely isotropic rheology of Johnson (1977), which approximates material (ice) parcels as axisymmetric with symmetry axis $\mathbf{m}$ (Fig. 1a). In the two-dimensional (2-D) case, the rotational symmetry about $\mathbf{m}$ reduces to a reflectional symmetry about $\mathbf{m}$, and the flow law becomes (Rathmann and others, 2021)

$$\boldsymbol{\tau} = \eta \Big[E_{mt}^{-2/(n+1)} \dot{\boldsymbol{\epsilon}} \\ + \Big(E_{mm}^{-2/(n+1)} - E_{mt}^{-2/(n+1)} \Big)(\dot{\boldsymbol{\epsilon}} \cdot\!\cdot\, \mathbf{m}\mathbf{m})(2\mathbf{m}\mathbf{m} - \mathbf{I}) \Big], \tag{1}$$

$$\eta = A^{-1/n} \Big[E_{mt}^{-2/(n+1)} \dot{\boldsymbol{\epsilon}} \cdot\!\cdot\, \dot{\boldsymbol{\epsilon}} \\ + 2\Big(E_{mm}^{-2/(n+1)} - E_{mt}^{-2/(n+1)} \Big)(\dot{\boldsymbol{\epsilon}} \cdot\!\cdot\, \mathbf{m}\mathbf{m})^2 \Big]^{(1-n)/2n}. \tag{2}$$

Here, $\boldsymbol{\tau}$ and $\dot{\boldsymbol{\epsilon}} = (\nabla \mathbf{u} + (\nabla \mathbf{u})^T)/2$ are the bulk deviatoric stress and strain rate tensors, A is the usual isotropic rate factor, and n is the power-law exponent. The bulk directional enhancement factors E_{mm} and E_{mt} are the strain rate enhancements for compression/extension along $\mathbf{m}$ and shear parallel to the plane with normal $\mathbf{m}$ (Fig. 1a), which follows from the forward rheology (not shown):

$$\dot{\epsilon}_{mm} = \dot{\boldsymbol{\epsilon}} \cdot\!\cdot\, \mathbf{m}\mathbf{m} = E_{mm}^{2/(n+1)} \eta^{-1} \tau_{mm}, \tag{3}$$

$$\dot{\epsilon}_{mt} = \dot{\boldsymbol{\epsilon}} \cdot\!\cdot\, \mathbf{m}\mathbf{t} = E_{mt}^{2/(n+1)} \eta^{-1} \tau_{mt}, \tag{4}$$

where $\mathbf{t}$ denotes any direction transverse to $\mathbf{m}$, and the indices m and t indicate the tensorial components in the directions of $\mathbf{m}$ and $\mathbf{t}$, respectively. In the limit of $E_{mm} = E_{mt} = 1$, Johnson's flow law reduces to Glen's flow law, representing isotropic ice. The enhancement-factor exponent $2/(n+1)$ ensures that the components $\dot{\epsilon}_{mm}$ and $\dot{\epsilon}_{mt}$ in Johnson's law, relative to those in Glen's isotropic law, are by definition E_{mm} and E_{mt}, respectively.

Bulk directional enhancement factors

Calculating E_{mm} and E_{mt} for a local ice parcel can be regarded as a problem of forming a suitable average over the parcel
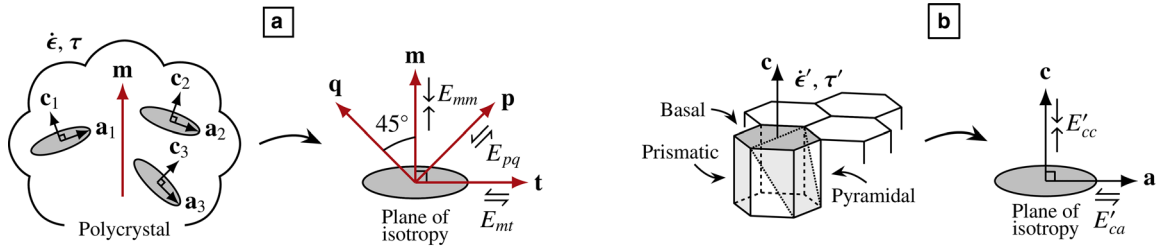
Fig. 1. (a) Axisymmetric polycrystal with longitudinal (E_{mm}), shear (E_{mt}), and $45°$-shear (E_{pq}) bulk enhancement factors with respect to the symmetry axis **m**. The transverse direction, **t**, lies in the plane of isotropy (**t**⊥**m**), while **p** is oriented at $45°$ to **m** and **p**⊥**q**. (b) Monocrystal lattice composed of hexagonal cells. Three crystallographic planes are highlighted in grey, where the c-axis indicates the basal-plane normal direction. Monocrystals are modelled as a transversely isotropic material with symmetry axis **c** and longitudinal (E'_{cc}) and shear (E'_{ca}) enhancement factors with respect to **c**. The transverse direction, **a**, lies in the plane of isotropy (**a**⊥**c**).

(polycrystal). A popular approach is to regard polycrystals as an ensemble of interactionless monocrystals (e.g. Castelnau and Duval, 1994; Svendsen and Hutter, 1996; Gödert and Hutter, 1998; Thorsteinsson, 2001). In this case, E_{mm} and E_{mt} follow from the monocrystal rheology by averaging over all grain orientations. Recognising that monocrystals deform 100–1000 times easier by basal plane shear (planes with normal **c**) than along any other crystallographic plane (Weertman, 1973; Duval and others, 1983), monocrystals have previously been approximated as transversely isotropic too (e.g. Meyssonnier and Philip, 1996; Svendsen and Hutter, 1996; Staroszczyk and Gagliardini, 1999). Following previous work, we therefore model the monocrystal rheology by a three-dimensional (3-D) but linear Johnson law:

$$
\dot{\boldsymbol{\epsilon}}' = A'\Bigg(\boldsymbol{\tau}' - \frac{E'_{cc} - 1}{2}(\boldsymbol{\tau}' \cdot\cdot \, \mathbf{cc})\mathbf{I}
$$
$$
+ \frac{3(E'_{cc} - 1) - 4(E'_{ca} - 1)}{2}(\boldsymbol{\tau}' \cdot\cdot \, \mathbf{cc})\mathbf{cc} \tag{5}
$$
$$
+ (E'_{ca} - 1)(\boldsymbol{\tau}' \cdot \mathbf{cc} + \mathbf{cc} \cdot \boldsymbol{\tau}')\Bigg),
$$

where $\boldsymbol{\tau}'$ and $\dot{\boldsymbol{\epsilon}}'$ are the microscopic deviatoric stress and strain rate tensors, A' is an isotropic rate factor, and the enhancement factors E'_{cc} and E'_{ca} are the strain rate enhancements for compression/extension along **c** and shear parallel to basal planes (Fig. 1b), i.e. $\dot{\epsilon}'_{cc} = A'E'_{cc}\tau'_{cc}$ and $\dot{\epsilon}'_{ca} = A'E'_{ca}\tau'_{ca}$.

In the simplest case, the grain-averaged rheology, $\langle\dot{\boldsymbol{\epsilon}}'(\boldsymbol{\tau}')\rangle$, may be constructed by assuming a uniform stress field over the polycrystal scale equal to the bulk stress (Sachs hypothesis), that is $\boldsymbol{\tau}' = \boldsymbol{\tau}$ and hence $\langle\dot{\boldsymbol{\epsilon}}'(\boldsymbol{\tau}')\rangle = \langle\dot{\boldsymbol{\epsilon}}'(\boldsymbol{\tau})\rangle$. The average is defined as

$$
\langle\dot{\boldsymbol{\epsilon}}'(\boldsymbol{\tau})\rangle_{\psi(\theta,\phi)} = \frac{1}{N}\int_{S^2}\dot{\boldsymbol{\epsilon}}'(\boldsymbol{\tau})\psi(\theta,\phi)\mathrm{d}\Omega, \tag{6}
$$

where $\psi(\theta,\phi)$ is the grain number distribution in orientation space S^2, $\mathrm{d}\Omega = \sin(\theta)\mathrm{d}\theta\mathrm{d}\phi$ is the infinitesimal solid angle, and $N = \int_{S^2}\psi(\theta,\phi)\mathrm{d}\Omega$ is the total number of grains. Unless stated otherwise, $\langle\cdot\rangle = \langle\cdot\rangle_{\psi(\theta,\phi)}$ is henceforth assumed implicit. Inserting Eqn (5) into Eqn (6), gives

$$
\langle\dot{\boldsymbol{\epsilon}}'(\boldsymbol{\tau})\rangle = A'\Bigg(\boldsymbol{\tau} - \frac{E'_{cc} - 1}{2}(\boldsymbol{\tau} \cdot\cdot \, \langle\mathbf{c}^2\rangle)\mathbf{I}
$$
$$
+ \frac{3(E'_{cc} - 1) - 4(E'_{ca} - 1)}{2}\boldsymbol{\tau} \cdot\cdot \, \langle\mathbf{c}^4\rangle \tag{7}
$$
$$
+ (E'_{ca} - 1)(\boldsymbol{\tau} \cdot \langle\mathbf{c}^2\rangle + \langle\mathbf{c}^2\rangle \cdot \boldsymbol{\tau})\Bigg),
$$

where $\langle\mathbf{c}^k\rangle = 1/N\int_{S^2}\mathbf{c}^k\psi(\theta,\phi)\mathrm{d}\Omega$ is the k-th order structure tensor. Provided with $\langle\dot{\boldsymbol{\epsilon}}'(\boldsymbol{\tau})\rangle$, Thorsteinsson (2001) suggested defining the bulk enhancement of the **v**–**w** component of $\dot{\boldsymbol{\epsilon}}$ as (**v** and **w** being arbitrary vectors)

$$
E_{vw}^{\mathrm{Sachs}}(\boldsymbol{\tau}) = \frac{\langle\dot{\boldsymbol{\epsilon}}'(\boldsymbol{\tau})\rangle \cdot\cdot \, \mathbf{vw}}{\langle\dot{\boldsymbol{\epsilon}}'(\boldsymbol{\tau})\rangle_{\mathrm{const.}} \cdot\cdot \, \mathbf{vw}}, \tag{8}
$$

where $\langle\dot{\boldsymbol{\epsilon}}'(\boldsymbol{\tau})\rangle_{\mathrm{const.}}$ is the average strain rate tensor of an isotropic polycrystal ($\psi(\theta,\phi) = \mathrm{const.}$).

In contrast to the Sachs hypothesis, the Taylor hypothesis assumes a constant strain rate over the polycrystal scale equal to the bulk strain rate, that is $\dot{\boldsymbol{\epsilon}}' = \dot{\boldsymbol{\epsilon}}$ and hence $\langle\boldsymbol{\tau}'(\dot{\boldsymbol{\epsilon}}')\rangle = \langle\boldsymbol{\tau}'(\dot{\boldsymbol{\epsilon}})\rangle$. In order to determine E_{vw} using Taylor's hypothesis, $\langle\boldsymbol{\tau}'(\dot{\boldsymbol{\epsilon}})\rangle$ must be posed in the inverse form $\dot{\boldsymbol{\epsilon}}(\langle\boldsymbol{\tau}'\rangle)$, given which

$$
E_{vw}^{\mathrm{Taylor}}(\langle\boldsymbol{\tau}'\rangle) = \frac{\dot{\boldsymbol{\epsilon}}(\langle\boldsymbol{\tau}'\rangle) \cdot\cdot \, \mathbf{vw}}{\dot{\boldsymbol{\epsilon}}(\langle\boldsymbol{\tau}'\rangle_{\mathrm{const.}}) \cdot\cdot \, \mathbf{vw}}. \tag{9}
$$

The reader is referred to Appendix A on how to determine $\dot{\boldsymbol{\epsilon}}(\langle\boldsymbol{\tau}'\rangle)$.

The realised stress and strain rate fields inside polycrystals are meanwhile between the two end-member cases of either field being homogeneous, although some observations and experiments (Azuma and Higashi, 1985; Azuma, 1995) suggest that the Sachs assumption is the better approximation of the two. As an alternative to more sophisticated homogenisation schemes, such as the viscoplastic self-consistent compromise between the Sachs and Taylor assumptions (Meyssonnier and Philip, 1996), we model E_{vw} as a simple linear combination of the Sachs and Taylor behaviour:

$$
E_{vw}(\boldsymbol{\tau}) = (1 - \alpha)E_{vw}^{\mathrm{Sachs}}(\boldsymbol{\tau}) + \alpha E_{vw}^{\mathrm{Taylor}}(\boldsymbol{\tau}), \tag{10}
$$

where the weight $\alpha \in [0; 1]$ is taken to be a free but constant parameter. In summary, model (10) has three free parameters (E'_{cc}, E'_{ca}, and α) and depends on the fields ψ and $\boldsymbol{\tau}$.

Constraining the free grain parameters
E_{mm} and E_{mt} are by definition the bulk enhancement factors of a polycrystal when subject to bulk pure- and simple-shear stresses with respect to **m** and **t**:

$$
E_{mm} = E_{mm}(\tau_0[\mathbf{I}/3 - \mathbf{mm}]), \tag{11}
$$

$$
E_{mt} = E_{mt}(\tau_0[\mathbf{mt} + \mathbf{tm}]), \tag{12}
$$

where τ_0 is an arbitrary stress magnitude that cancels by virtue of the division in Eqns (8) and (9), as does A'. Deformation tests
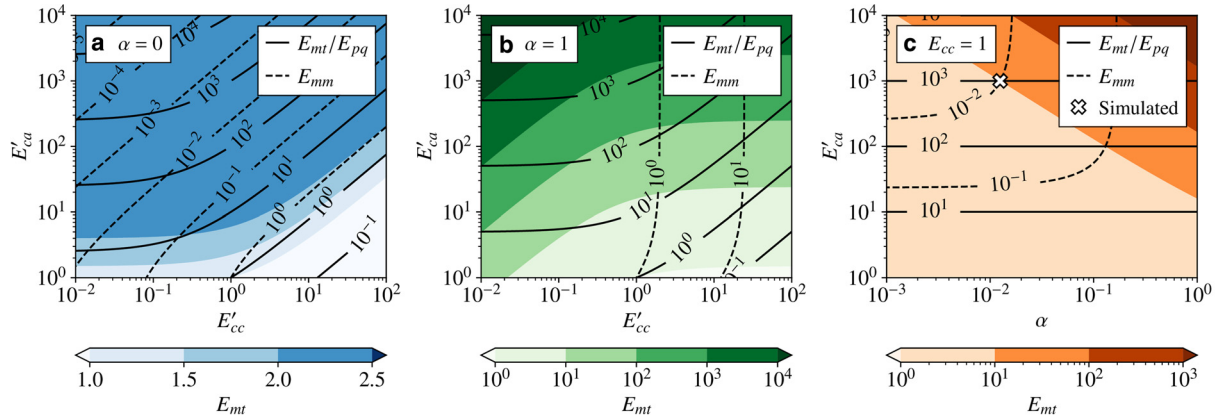
Fig. 2. Bulk enhancement factors E_{mt} (coloured contours), E_{mm} (dashed contours), and E_{mt}/E_{pq} (solid contours) for a unidirectional orientation fabric ($\mathbf{c} = \mathbf{m}$) as a function of the grain enhancement factors E'_{cc} and E'_{ca} in the case of (a) the Sachs model, (b) the Taylor model, and (c) a linear combination of the Sachs and Taylor models depending on α (assuming grains are equally hard to compress along $\mathbf{c}$ and $\mathbf{a}$, implying $E'_{cc} = 1$). The cross in panel c indicates the grain parameters used to model the bulk enhancement factors in our ice-flow simulations. Note the colourbar scale is linear in panel a, as opposed to in panel b and panel c, because E_{mt} varies less in the Sachs model (see main text).

conducted on ice samples with strong single-maximum fabrics (aligned c-axes) suggest that $E_{mt} \simeq 10$ (Pimienta and others, 1987) and $E_{mt}/E_{pq} \simeq 10^3$ to 10^4 (Shoji and Langway, 1985, 1988), where $E_{pq} = E_{pq}(\tau_0[\mathbf{pq} + \mathbf{qp}])$ and $\mathbf{p} = (\mathbf{m} + \mathbf{t})/\sqrt{2}$ and $\mathbf{q} = (\mathbf{m} - \mathbf{t})/\sqrt{2}$ (see Fig. 1a).

Figures 2a, b show the Sachs ($\alpha = 0$) and Taylor ($\alpha = 1$) bulk enhancement factors E_{mt} (coloured contours), E_{mm} (dashed black contours), and E_{mt}/E_{pq} (solid black contours) for a unidirectional fabric ($\mathbf{c} = \mathbf{m}$) as a function of the grain parameters E'_{cc} and E'_{ca}. In line with past studies, the Sachs model is limited in how strong E_{mt} can become, and the Taylor model in how strong E_{mm} can become (see Gillet-Chaulet and others (2005) and references therein). Following Gillet-Chaulet and others (2005) by setting $E'_{cc} = 1$ (grains are equally hard to compress along $\mathbf{c}$ and $\mathbf{a}$), Fig. 2c shows the resulting bulk enhancements as a function of E'_{ca} and α. On setting $(E'_{cc}, E'_{ca}, \alpha) = (1, 10^3, 0.0125)$, the model (10) is able to reproduce the experimentally determined bulk enhancements mentioned above, which implies $E_{mm} = 10^{-2}$. Note that small values of α are consistent with the Sachs hypothesis being approximately true (at least as far as mechanical strength of polycrystals is concerned).

We mention in passing that the rheology of monocrystals has experimentally been found to follow a power law with an orientation-dependent non-linear viscosity (Kamb, 1961; Duval and others, 1983). If the linear-viscous grain rheology (5) is assumed, bulk enhancements can be up to an order of magnitude weaker for intermediate-to-strong fabrics in the Sachs limit (8) (Rathmann and others, 2021). By including the α-weighted Taylor contribution, the linear-viscous model (10) reproduces the experimentally derived bulk enhancements for strong fabrics (which neither the Sachs nor Taylor model can accomplish alone), and thus is taken to suffice for our purpose although it might too deviate from the non-linear values for intermediate-strength fabrics.

Fabric evolution

Simulating the flow of anisotropic ice requires solving a coupled time-dependent problem involving the velocity and fabric fields, $\mathbf{u}(\mathbf{x}, t)$ and $\psi(\mathbf{x}, t, \theta, \phi)$. Under cold and low-stress conditions, the orientation fabric of an ice parcel is predominantly a function of its strain history (Alley, 1988). That is, the strain-induced rotation of c-axes, or *lattice rotation*, accounts for the tendency of grain c-axes to rotate towards the compressive axis and away from the extensional axis (Azuma and Higashi, 1985; van der Veen and Whillans, 1994), consistent with ice cores drilled at cold, low strain rate locations (Faria and others, 2014b). Under

warm (typically $-10\,^{\circ}$C or above) and high-stress conditions, however, the orientation fabric is, instead, predominantly a function of dynamic recrystallisation processes that depend on the in situ stress state (Duval and Castelnau, 1995). In this case, grains nucleate in regions of high-lattice distortion, which is a process considered to work in conjunction with migration recrystallisation for explaining the recovery of distorted lattices; that is, newly formed strain-free nuclei grow at the expense of consuming older, more strained grains (De La Chapelle and others, 1998). Because grains nucleate with c-axis orientations favourable for deformation by basal glide (Kamb, 1972), the resulting fabrics can differ considerably from those produced by lattice rotation alone (Alley, 1992), and hence possibly change the local directional viscosity structure resulting from lattice rotation.

In our ice-flow model, we consider non-negligible sliding at the ice–bed interface, which is commonly associated with relatively warm near-bed temperatures. For this reason, we investigate both end-member cases where fabric evolution is dominated by either lattice rotation or dynamic recrystallisation near the bed. Polygonisation is neglected throughout; a recrystallisation process which accounts for the division of grains along internal sub-grain boundaries when exposed to bending stresses (Alley and others, 1995). In effect, polygonisation reduces the average grain size upon grain division but does not necessarily change the orientation fabric much (Alley, 1992). Strictly speaking, we therefore consider only discontinuous dynamic recrystallisation (DDRX), understood as the combined effect of nucleation and migration recrystallisation.

Lattice rotation

We model lattice rotation using our spectral fabric model (Rathmann and others, 2021). The model is a kinematic model in the sense that c-axes rotate in response to the bulk stretching, $\dot{\boldsymbol{\epsilon}}$, and spin, $\boldsymbol{\omega} = (\nabla \mathbf{u} - (\nabla \mathbf{u})^T)/2$, thereby allowing the detailed microscopic stress and strain rate fields to be neglected and hence interactions between neighbouring grains to be disregarded. By moreover requiring that basal planes preserve their orientation when subject to simple shear (like a deck of cards), the rotation of an arbitrary c-axis $\mathbf{c} = \mathbf{c}(\theta, \phi) = [\sin(\theta)\cos(\phi), \sin(\theta)\sin(\phi), \cos(\theta)]$ is modelled as (Castelnau and others, 1996; Svendsen and Hutter, 1996; Gödert and Hutter, 1998)

$$\dot{\mathbf{c}} = (\boldsymbol{\omega} - \dot{\boldsymbol{\epsilon}} \cdot \mathbf{cc} + \mathbf{cc} \cdot \dot{\boldsymbol{\epsilon}}) \cdot \mathbf{c}. \tag{13}$$

The corresponding effect on the (continuous) number distribution, ψ, is modelled as a conservative advection process on S^2

involving the *c*-axis velocity field $\dot{\mathbf{c}}(\theta, \phi)$ (Gödert and Hutter, 1998):

$$\frac{D\psi}{Dt} + \nabla_{S^2} \cdot (\psi\dot{\mathbf{c}}) = 0, \tag{14}$$

where D/D*t* is the material derivative, and the divergence operator acts on S^2.

Note that existing fabric models that focus on the time evolution of $\langle \mathbf{c}^2 \rangle$ (effectively a low-order representation of ψ) have previously found a kinematic approach to be sufficient for reproducing observed fabric eigenvalue trends in ice cores (Gillet-Chaulet and others, 2006; Durand and others, 2007; Martín and others, 2009), a result that our model reproduces for the GRIP ice-core fabric (Thorsteinsson and others, 1997) (not shown).

Dynamic recrystallisation

We model DDRX (nucleation and migration recrystallisation) as a single, spontaneous decay process on S^2 following Placidi and others (2010):

$$\frac{D\psi}{Dt} = \Gamma\psi, \tag{15}$$

where $\Gamma = \Gamma(\theta, \phi)$ is the orientation decay rate. In this way, the orientation density increases locally on S^2 where $\Gamma(\theta, \phi) > 0$, and decreases where $\Gamma(\theta, \phi) < 0$.

The *c*-axes of nucleated grains tend to align with the direction that maximises the resolved basal plane shear stress, $\boldsymbol{\tau} \cdot \mathbf{c} - (\boldsymbol{\tau} \cdots \mathbf{cc})\mathbf{c}$, thus favouring deformation by basal glide. Placidi and others (2010) proposed that

$$\Gamma = \Gamma_0(D - \langle D \rangle), \tag{16}$$

where Γ_0 is a DDRX rate factor that depends on the local temperature, dislocation density, and stress state. The deformability, D, is the normalised square of the resolved shear stress

$$D(\mathbf{c}, \boldsymbol{\tau}) = \frac{(\boldsymbol{\tau} \cdot \boldsymbol{\tau}) \cdots \mathbf{c}^2 - \boldsymbol{\tau} \cdots \mathbf{c}^4 \cdots \boldsymbol{\tau}}{\boldsymbol{\tau} \cdots \boldsymbol{\tau}}, \tag{17}$$

which is strictly positive. The average deformability, $\langle D \rangle$, provides a threshold for the deformability, D, below which orientations decay, and above which are produced. Formally speaking, $\langle D \rangle$ is a Lagrange multiplier that ensures the total number of grains, $N = \int_{S^2} \psi \, d\Omega$, is conserved, which follows directly from calculating the material derivative

$$\frac{DN}{Dt} = \Gamma_0 \int_{S^2} D\psi \, d\Omega - \Gamma_0 N \langle D \rangle = 0. \tag{18}$$

In reality, however, it is the total mass that is conserved, not N. Nonetheless, in the absence of more sophisticated models, Eqn (16) provides a useful model to explore the major effect of DDRX, here understood as the orientation-dependent nucleation and consumption of grains as a function of $\boldsymbol{\tau}$.

For reference, the decay rate Eqn (16) is plotted in Fig. 3 in the case of unconfined uniaxial compression along $\hat{\mathbf{z}}$ (panel a), uniaxial compression along $\hat{\mathbf{x}}$ with extension confined to $\hat{\mathbf{z}}$ (panel b), and simple $\hat{\mathbf{x}}$–$\hat{\mathbf{z}}$ shear (panel c). Note that Γ depends on the instantaneous value of ψ by virtue of $\langle D \rangle$, which was taken to be isotropic in Fig. 3. Red and blue colours indicate the directions for which orientations are produced (grain nucleates) and decay (grains consumed), respectively. Although the case of unconfined uniaxial compression (Fig. 3a) is relevant for the stress regimes found near ice domes, the latter cases of confined compression and vertical shear are relevant for the stress regimes realised in our ice-flow simulations.

Representation

We represent the grain number distribution by a series expansion in spherical harmonic functions, $Y_l^m(\theta, \phi)$:

$$\psi(\mathbf{x}, t, \theta, \phi) = \sum_{l=0}^{L} \sum_{m=-l}^{l} \psi_l^m(\mathbf{x}, t) Y_l^m(\theta, \phi), \tag{19}$$

where the expansion coefficients, ψ_l^m, constitute the fabric model unknowns (degrees of freedom), and L is the wave-mode truncation above which finer-scale structure in ψ is unresolved. We defer the reader to the Appendix for further details on how lattice rotation and DDRX affect the time-evolution of ψ_l^m.

We end by noting that for expansion (19), the entries of the structure tensors $\langle \mathbf{c}^2 \rangle$ and $\langle \mathbf{c}^4 \rangle$ – required to calculate E_{mm} and E_{mt} – are given by linear combinations of ψ_l^m for $l \leq 4$ (Advani and Tucker, 1987; Rathmann and others, 2021).

Numerical experiments

We are interested in the extent to which the true basal drag or friction coefficient field can be inferred by an inversion procedure if ice is assumed isotropic when *in fact it is not*. For this purpose, we consider two idealised vertical slab models that are 40 km long and 2 km tall, placed on a $0.3°$ inclined plane (approximately the surface slope over the Northeast Greenland Ice Stream) with periodic left–right boundaries.

Both models are subject to a Weertman sliding law along the basal boundary, Γ_b:

$$\mathbf{t}_b = -f^2 \|\mathbf{u}_b\|^{1/m-1} \mathbf{u}_b, \tag{20}$$

where $\mathbf{t}_b = \boldsymbol{\sigma} \cdot \hat{\mathbf{n}} - (\boldsymbol{\sigma} \cdots \hat{\mathbf{n}}\hat{\mathbf{n}})\hat{\mathbf{n}}$ is the basal shear stress, $\mathbf{u}_b$ is the basal sliding velocity, $f = f(x)$ is the square root of the friction-coefficient field, m is the sliding-law exponent, and $\hat{\mathbf{n}}$ and $\hat{\mathbf{r}}$ are the boundary normal and tangential directions, respectively. No melting is assumed at the ice–bed boundary and therefore $\mathbf{u}_b \parallel \hat{\mathbf{r}}$. We considered both linear sliding, $m = 1$, and non-linear hard-bedded sliding, $m = 3$. However, because the resulting fabric development is largely the same (not shown, discussed below), we focus on the results for $m = 1$. Whether fabric evolves similarly in the Coulomb-plastic limit, which recent work has shown to be relevant for weak beds such as deformable till (Joughin and others, 2019) and perhaps for hard beds (Zoet and Iverson, 2020), was not considered. On that note, we re-emphasise that our study is concerned with flow regimes where both sliding and internal deformation are non-negligible. In the case of e.g. fast-sliding ice streams and marine outlets, the sliding is likely affected by the effective pressure at the bed (e.g. Brondex and others, 2019), and the possibility of reduced shear stresses/strains (increased longitudinal stresses/strains) due to sliding may cause fabric development different from that reported here.

The free-surface height, $s(x, t)$, is allowed to evolve the usual way according to the local mass convergence (no accumulation or melting assumed)

$$\dot{s} = u_z^s - u_x^s \frac{\partial s}{\partial x}, \tag{21}$$

where $u_x^s = u_x(x, s(x, t))$ and $u_z^s = u_z(x, s(x, t))$ are the surface velocity components.

The first model (Fig. 4a) investigates the effect of a sticky spot, defined as a local increase in the friction coefficient (strictly
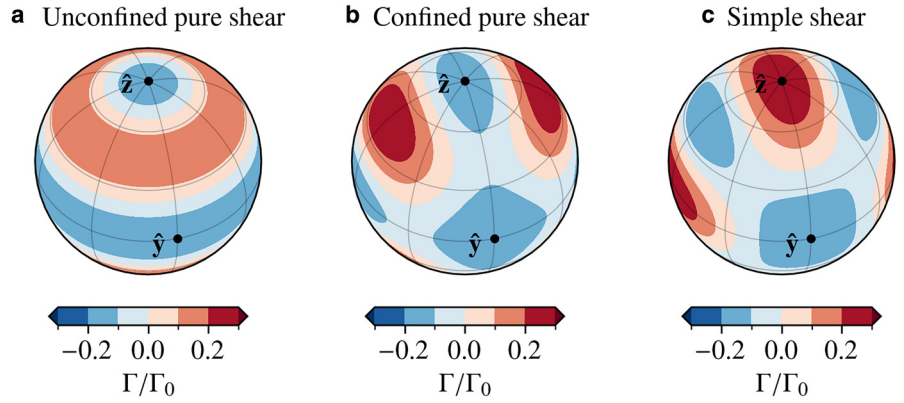
a Unconfined pure shear   **b** Confined pure shear   **c** Simple shear

Fig. 3. Orientation decay rate functions for DDRX in the case of unconfined uniaxial compression along $\hat{z}$ (a), uniaxial compression along $\hat{x}$ with extension confined to $\hat{z}$ (b), and simple $\hat{x}$–$\hat{z}$ shear (c). Positive (red) and negative (blue) areas indicate the directions for which orientations are produced (grain nucleates) and decay (grains consumed), respectively.

a Sticky spot model   **b** Bed bump model
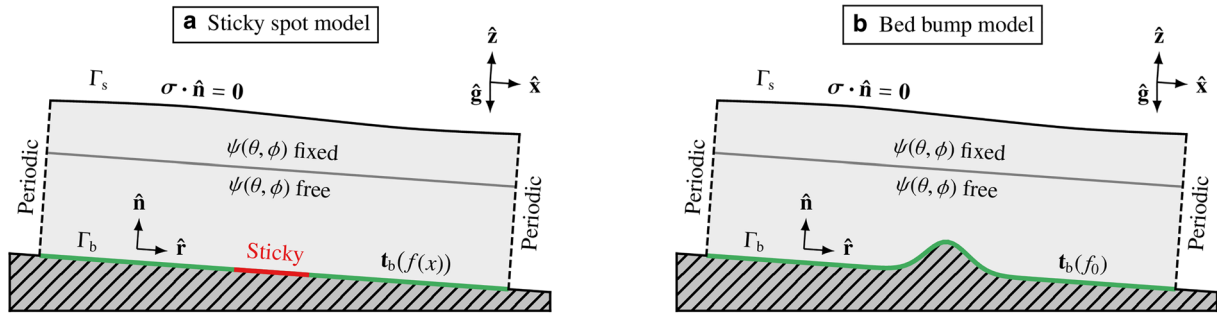
Fig. 4. Ice-flow model configuration and boundary conditions used in the (a) sticky spot and (b) bed bump numerical experiments.

speaking a flow-transverse sticky line). Specifically, we consider a sticky spot on a flat bed, given by the centred Gaussian profile

$$f^2(x) = f_0^2 - \left(f_0^2 - f_1^2\right) \exp\left[\frac{-(x - 20\,000\,\mathrm{m})^2}{2\,000\,000\,\mathrm{m}^2}\right], \quad (22)$$

where the peak value, f_1^2, is taken to be 100 times that of the surrounding constant background value of $f_0^2 = 5 \times 10^{10}\,\mathrm{Pa\,s\,m^{-1}}$. The value of f_0^2 was selected to allow for moderate sliding on the order of 20 % of the modelled surface velocities, although a larger and smaller sliding ratios was also considered (see 'Discussion'). The second model (Fig. 4b) investigates the effect of a bed bump (strictly speaking a lateral ridge) with an amplitude of $b_1 = 200$ m (10% of the ice thickness), given by the centred Gaussian bed profile

$$b(x) = b_1 \exp\left[\frac{-(x - 20\,000\,\mathrm{m})^2}{2\,000\,000\,\mathrm{m}^2}\right], \quad (23)$$

but with a uniform friction coefficient of $f^2(x) = f_0^2$. In both models, wider asperities where also considered (see 'Discussion').

The rate of DDRX, Γ_0, depends in principle on the local temperature, dislocation density, and stress state. Although Richards and others (2021) recently explored possible functional forms of Γ_0, we shall, for simplicity, consider the two cases where fabric evolution is dominated near the bed by either lattice rotation or DDRX. Specifically, one experiment assumes lattice rotation without DDRX by setting $\Gamma_0 = 0$, while the other assumes lattice rotation with active DDRX by setting

$$\Gamma_0(z) = \begin{cases} 0 & \text{for } z > H_\Gamma \\ (1 - z/H_\Gamma)10^{-8}\,\mathrm{s^{-1}} & \text{for } z \leq H_\Gamma, \end{cases} \quad (24)$$

taken to represent gradually warming ice between $z = H_\Gamma$ and $z = 0$

(the bed). Indeed, within a temperature range of -30 to $-5\,^{\circ}$C, Richards and others (2021) found that Γ_0 depends approximately linearly on temperature. Here, we set $H_\Gamma = 2000$ m/3 to confine DDRX to the lower third of the ice mass. Note that Γ_0 simply sets the DDRX timescale, representing the relative strength of DDRX to lattice rotation in our model. With Eqn (24), the fabric evolves and saturates $\sim$5 times faster in our simulations compared to when lattice rotation acts alone, and DDRX is therefore regarded to be the dominant process.

In summary, four forward experiments are considered, consisting of two kinds of model geometries (Fig. 4) in which DDRX is either negligible or dominant in the lower third of the ice mass.

Forward simulations

The full Stokes momentum balance was solved for all four forward models using Johnson's flow law with $n = 3$ and $A = 3.5 \times 10^{-25}\,\mathrm{s^{-1}\,Pa^{-3}}$ (corresponding to isothermal ice at $\sim -10\,^{\circ}$C) until a steady fabric state was reached, taking approximately 100 a and 500 a with and without DDRX, respectively. Although real temperature distributions in glaciers and ice sheets are not isothermal, our aim is to investigate (in isolation) the effect of mechanical anisotropies induced by fabric, whereas temperature heterogeneities affect the viscosity isotropically through the flow-rate factor $A = A(T)$. Insofar as the temperature is high enough to affect the rate of DDRX, temperature can indirectly induce mechanical anisotropies, which Eqn (24) attempts to represent (albeit rather simplistically without a thermal coupling).

The fabric fields were initialised uniformly to match the GRIP surface state (not shown), corresponding to a weak vertical single maximum. In the upper 30 % of the model domains, the (initial) fabric field was held fixed throughout time. In addition to ensuring that ice is approximately isotropic at the surface, this fabric slab boundary condition allows for the fabric to reach steady state much faster than without; weak shear strain rates in the

near-surface cause fabric to develop much slower than below. Note, however, that this choice does not affect the steady-state fabric solution below, nor does it affect our conclusions.

The momentum balance, surface evolution, and fabric evolution were solved using a backward Euler (implicit) time-stepping scheme with a step size of $\Delta t = 0.5$ a, a Taylor–Hood finite-element discretisation of position space on a structured triangular mesh with a grid size of $(\Delta x, \Delta z) = (600 \text{ m}, 120 \text{ m})$ refined to $(\Delta x, \Delta z) = (200 \text{ m}, 60 \text{ m})$ within $15 \text{ km} \le x \le 25 \text{ km}$ and $0 \text{ km} \le y \le 1 \text{ km}$, and a spectral discretisation of orientation space truncated at $L = 10$. For $L = 10$, the regularisation selected in orientation-space (see Appendix C) is 30 times stronger for modes ψ_l^m with $l = 10$ compared to $l = 4$, thereby significantly reducing the effect of regularisation on the modes that E_{mt} and E_{mm} depend upon ($l \le 4$). The truncation implies a 66-dimensional linear advection–reaction–diffusion problem must be solved per computational node in order to evolve the fabric field. In terms of traditional structure-tensor-based fabric models, $L = 10$ corresponds to simulating all even-ordered structure tensors through order ten. The entire system was solved using FEniCS (Logg and others, 2012), relying on Newton's method to solve the non-linear momentum balance. The Jacobian of the residual form (required for Newton iterations) was calculated using the unified form language (UFL) (Alnæs and others, 2014), used by FEniCS to specify weak forms, which supports automatic symbolic differentiation. The weak forms are presented in Appendix C.

Inversions

Basal friction
Selecting the four Johnson steady states as the 'true' states, we attempt to invert for $f(x)$ using Glen's flow law and compare the results to the true friction fields, and to results obtained from inversions using Johnson's flow law (the 'true' rheology). All remaining parts of the problem are assumed perfectly known (bedrock height, surface height, surface velocities, and the fabric field).

We emphasise that inverting for f using Johnson's flow law is only feasible for synthetic experiments, and not in practice, since the true fabric state is generally unknown for real glaciers where inversions are performed. Our aim is, however, to assess the *type* of error introduced by assuming fabric isotropy by virtue of Glen's flow law, which the comparison allows. In this way, re-inferring f with Johnson's law serves as a best-case scenario with which to compare the Glen-based inversions (elaborated on below). If Johnson's flow law is to be used for inversions over real glaciers, a more formal investigation is needed to clarify the effects that imperfect knowledge of fabric, bed and surface profiles, and surface velocities have.

We invert for $f(x)$ using the canonical method by MacAyeal (1993) and Joughin and others (2004) of reducing the surface-velocity misfit by minimising an appropriate cost functional. Following ice-flow models such as Úa (Gudmundsson and others, 2012; Ranganathan and others, 2020), we adopt the cost functional

$$J(\mathbf{u}(f), f) = \int_{\Gamma_s} \| \boldsymbol{\beta} \cdot (\mathbf{u}(f) - \mathbf{u}^{\text{true}}) \|^2 \, \mathrm{d}l + \gamma_f \int_{\Gamma_b} \left(\frac{\mathrm{d}f^2}{\mathrm{d}x} \right)^2 \mathrm{d}l, \quad (25)$$

which penalises both the surface-velocity misfit and large gradients in f^2, the former depending on the surface velocity uncertainties as prescribed by diagonal matrix $\boldsymbol{\beta}$, the latter depending on the magnitude of the regularisation parameter γ_f. Note that the 'true' velocity field is well-defined only for our synthetic experiments (taken to be the Johnson states), whereas for real inversions it is to be replaced by the observed velocity field. Since the true surface velocities are in fact known in synthetic experiments, $\boldsymbol{\beta} = \mathrm{diag}(1, 1)$

is arguably an appropriate choice. In the interest of being as generous as possible to Glen's flow law, we find, however, that signal-to-noise ratios in inferred f^2 are improved if vertical velocity errors are not penalised, i.e. $\boldsymbol{\beta} = \mathrm{diag}(1, 0)$. This choice is standard for inversions conducted over real glaciers and ice sheets (e.g. Morlighem and others, 2013), since often only horizontal velocities are available from satellite observations (e.g. Joughin and others, 2018). The conclusions drawn from the inferred f fields are effectively unchanged by this choice.

The problem of determining f such that $J(\mathbf{u}(f), f)$ is (locally) minimised was solved following a Newton conjugate gradient descent with a strong Wolfe line search. The cost functional gradient was evaluated with the adjoint-state method using dolfin-adjoint (Mitusch and others, 2019), a library which allows the adjoint equation to be derived and solved automatically for each gradient evaluation given a forward model in FEniCS.

All inversions were carried out with an initial guess of $f^2(x) = f_0^2/10$. As a stopping criterion we selected a relative change in the cost functional between two consecutive Newton steps of $<10^{-3}$ (beyond which further iterations provided negligible improvement), requiring up to 23 iterations depending on regularisation.

Isotropic enhancement factor
In addition to fabric anisotropy, the viscosity of glacier ice can locally be affected by e.g. ice temperature anomalies and impurities. Recognising this, some state-of-the-art parameter inversion in glaciology is concerned with jointly inferring both f^2 (or the equivalent thereof) and the flow-rate factor A (see e.g. Arthern, 2015; Isaac and others, 2015; Ranganathan and others, 2020). Without doing so, errors in the prescribed rate-factor field will manifest themselves in the inferred friction coefficient field (e.g. Arthern and others, 2015). However, since both f and A affect the surface velocity, without additional constraints this problem is generally underdetermined even for depth-averaged models where only one viscosity needs to be determined at each point in horizontal space.

Inferring A is clearly appropriate to account for isotropic flow-rate enhancements, such as those caused by temperature and impurity heterogeneities. The enhancements due to fabric are however inherently anisotropic, and the ability to represent these by inferring a (single) scalar field is less clear. For this reason, we additionally consider the possibility of *isotropically compensating* for fabric anisotropy by including an enhancement factor, $E(x, y)$, inspired by Gagliardini and others (2013) and the CAFFE model (Placidi and others, 2010). That is, by setting

$$A \rightarrow E(x, y)A, \quad (26)$$

can $E(x, y)$ be inferred such that Glen's law reproduces the true (observed) surface velocities given the true basal friction, f^2? If so, it would indicate that it is possible to isotropically infer the effect of fabric (e.g. when inferring the rate factor of ice shelves), and suggest that that jointly inferring f and A could recover (some) fabric effects, given that the underdeterminedness can be overcome.

Unless carefully posed, inferring E is an underdetermined problem for our non-depth-averaged model even when f is known: the field $E(x, y)$ is to be constrained given only the resulting surface velocities, but surface velocities may increase if any horizontal layer within is enhanced ($E > 1$). We therefore propose

inferring E by minimising the cost functional

$$
\begin{aligned}
J\big(\mathbf{u}(E), E\big) = & \int_{\Gamma_s} \big\| \boldsymbol{\beta} \cdot \big(\mathbf{u}(E) - \mathbf{u}^{\text{true}}\big) \big\|^2 \mathrm{d}l \\
& + \gamma_E \int w(z)(E - 1)^2 \mathrm{d}\mathbf{x} + \gamma_u \int_{\Gamma_s} \left(\frac{\mathrm{d}u_x(E)}{\mathrm{d}x} \right)^2 \mathrm{d}l,
\end{aligned}
\tag{27}
$$

where the first term penalises the surface-velocity misfit (identically to Eqn (25)), the second term is a depth-dependent penalisation of deviations from isotropy ($E \neq 1$), where the total (integrated) penalty is weighted by γ_E, and the third term penalises large gradients in u_x along the surface depending on the regularisation parameter γ_u. In this way, the purpose of the weight $w(z)$ is to constrain deviations from isotropy to occur primarily at depth where fabric anisotropy is presumably strongest. For our purpose, we set

$$
w(z) = 1 + 10 \frac{\tanh\big(5 \times 10^{-3}\,(z - 1000\,\mathrm{m})\big) + 1}{2},
\tag{28}
$$

which monotonically penalises anisotropy towards the surface ten times more than at the bed. A linearly increasing weight was also found to suffice, although convergence proved slower. The regularisation term (last term) in Eqn (27) leads to smoother and less noisy solutions for E. Although directly penalising gradients in E would have the same effect, the proposed regularisation was found to produce a faster and more reliable convergence.

The cost functional (27) was minimised using the same method as described above for Eqn (25). Inversions were carried out with an uniform initial guess of $E = 1$ (isotropy), and the free parameters were set to $\gamma_E = 5 \times 10^{-18}$ and $\gamma_u = 5 \times 10^{6}$. The parameter values were chosen such that the surface-velocity misfit was reasonable without over-fitting E: by further decreasing γ_u, E becomes noisy, and by increasing γ_E the cost of introducing anisotropy ($E \neq 1$) becomes too large to reduce the surface-velocity misfit. Although other parameter combinations are possible, the present values suffice for demonstrating that inverting for E is feasible, at least under fairly strong assumptions about the depths at which fabric affects the flow.

Results

Forward steady states

The forward steady states are shown in Figs 5, 6 in the case of lattice rotation without and with DDRX, respectively. Panels a1–c1 (left-hand column) and a2–c2 (right-hand column) show the results for the sticky spot (sticky line) and bed bump (lateral ridge) model, respectively. Panels a1 and a2 show the resulting steady-state flow speed (true friction field given) of the Johnson flow law, relative to that produced by Glen's law interpolated onto the same grid. Panels b1 and b2 show the ratio of x–z shear enhancement to x–x longitudinal (compressional/extensional) enhancement caused by the fabric. Panels c1 and c2 show the symmetry-axis vector field $\mathbf{m}$ (black arrows) and the associated eigenvalues a_m (contours). Because the fabric field consists everywhere of a single-maximum in all four simulations, $\mathbf{m}$ is identical to the largest eigenvalue direction, which approximately coincides with the vertical direction. Hence, $\mathbf{m} \simeq \hat{\mathbf{z}}$ and therefore $E_{mt} \simeq E_{xz}$ and $E_{mm} \simeq E_{xx}$. For reference, panels d1–e1 and d2–e2 show the corresponding orientation distribution functions, $\psi(\theta, \phi)/N$, at the near-bed locations marked in panels c1 and c2 (note the subtle differences on close inspection).

The results without DDRX show that the orientation fabric develops over the sticky spot in such a way as to locally enhance

deformation by shear and oppose longitudinal deformation (large E_{xz}/E_{xx} ratio in Fig. 5b1), resulting in significant horizontal gradients in the flow speed modelled by Johnson's law compared to (divided by) Glen's law (Fig. 5a1). Although the ratio E_{xz}/E_{xx} is weakened over the sticky spot when DDRX is active (Fig. 6b1), the resulting relative flow speed pattern over the asperity is unchanged (Fig. 6a1). That is, ice flows much faster over the sticky spot if fabric anisotropy is accounted for, both with and without DDRX. The E_{xz}/E_{xx} ratio is similarly large over the bed bump peak (Figs 5b2, 6b2), but the resulting relative speed (Figs 5a2, 6a2) does not indicate a large speed-up due to fabric, suggesting that any speed-up experienced as ice passes over the bump is to first-order well-captured by Glen's law. This is, however, not to say that fabric anisotropy is unimportant: fabric anisotropy still causes gradients in the (relative) surface speed, to which an inversion is sensitive.

Note that with the regularisation selected in orientation space, steady-state eigenvalues saturate ∼0.9–0.95 (panels c1 and c2), and the magnitude of E_{mt} and E_{mm} (and hence E_{xz}/E_{xx}) that can be achieved is therefore limited.

Inversions

Basal friction

Figures 7a1, a2 show the inferred profiles of $f^2(x)$ using Glen's (blue lines) and Johnson's (red lines) flow law compared to the true profile (black line) for the sticky spot and bed bump model, respectively. Without affecting conclusions, Fig. 7 shows only the results from inverting the DDRX-active simulations. To estimate the sensitivity of our results to the choice of γ_f, each inversion was carried out for a small ensemble of γ_f (see Fig. 7 legends). The corresponding basal drag ($\mathbf{t}_b$) and horizontal surface velocity component (u_x^s) are shown in panels b1, b2 and c1, c2, respectively. Panels d1 and d2 show the corresponding vertically integrated mass fluxes and are treated later in the 'Discussion'.

The results show that f^2 is underestimated if inverted for with Glen's law (blue lines compared to black in Figs 7a1, a2), whereas the true f^2 can be recovered if the (true) Johnson flow law is used, depending on the amount of regularisation. Of course, the Glen-based inversions can, without further ado, be evaluated by comparing with the true value of f^2. The purpose of including the Johnson-based inversions is simply to characterise the degree of regularisation (smoothing) that the Glen-based inversions are subject to; the Johnson-based inversions represent best-case scenarios for the Glen-based inversions. Note that in both models, the background value of f^2 (the equivalent of f_0^2) is not constant when inferred using Glen's law. This carries over to the resulting basal drag, too (Figs 7b1, b2).

Given the small surface-velocity misfit (Figs 7c1, c2), the discrepancies between the Johnson- and Glen-based inversions may be attributed to the effect of fabric anisotropy and are treated in the 'Discussion'.

Isotropic enhancement factor

Figures 8a, b show the inferred isotropic enhancement factor field, E, for the sticky spot and bed bump experiments with DDRX, respectively. Similar results are found for the lattice-rotation-only experiments. The inferred patterns conform with the softening suggested by the anisotropic enhancement factors and the relative flow speeds in Fig. 6. By dividing the shear $\dot{\epsilon}_{xz}(\boldsymbol{\tau} = \tau_0(\hat{\mathbf{x}}\hat{\mathbf{z}} + \hat{\mathbf{z}}\hat{\mathbf{x}}))$ and the longitudinal $\dot{\epsilon}_{xx}(\boldsymbol{\tau} = \tau_0(\mathbf{I}/2 - \hat{\mathbf{x}}\hat{\mathbf{x}}))$ strain rates resulting from Glen's law (E given) with those produced by Johnson's law (true fabric state given), we find that E to first-order captures the effective shear-strain rate enhancement (Figs 8c, d) at the expense of producing too soft ice when subject to longitudinal stresses (Figs 8e, f).
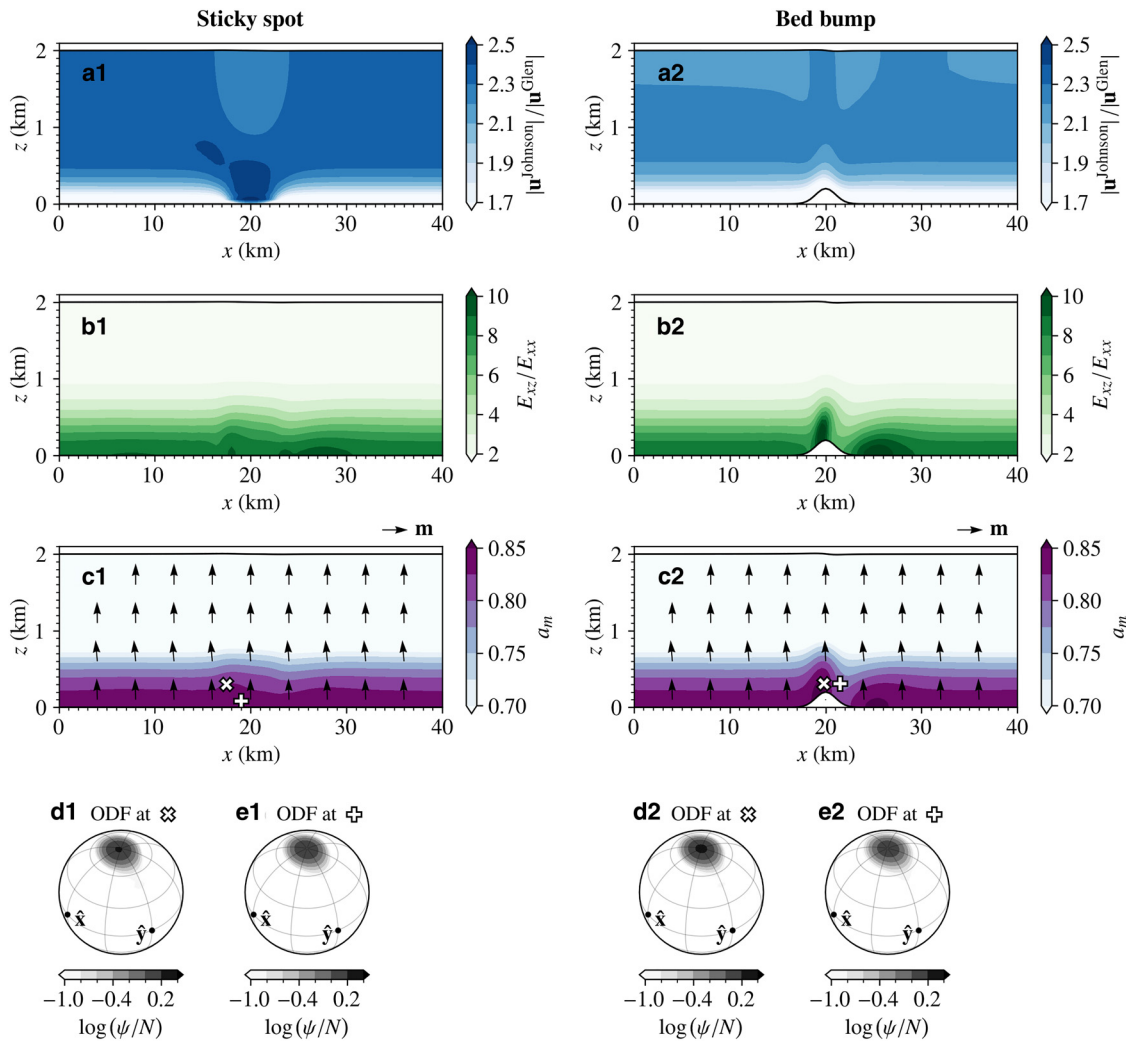
Fig. 5. Steady states of the sticky spot model (a1–e1) and the bed bump model (a2–e2) without DDRX. Panels a1 and a2 show the steady-state flow speed of the (forward) Johnson flow law, relative to that produced by Glen's law, given the true friction field, f. Panels b1 and b2 show the ratio of x–z shear enhancement to x–x compressional/extensional enhancement caused by the fabric. Panels c1 and c2 show the symmetry-axis vector field $\mathbf{m}$ (arrows) and associated eigenvalues a_m (contours). Panels d1, e1 and d2, e2 show the orientation distribution functions $\psi(\theta, \phi)/N$ at the locations marked in panels c1 and c2, respectively.

Figures 8g, h show the resulting horizontal surface-velocity profiles and vertically integrated mass fluxes, respectively. Although the surface velocity peaks are less well-captured (due to regularisation) compared to when inferring f alone, the resulting mass-flux errors are comparatively reduced.

Discussion

Our results suggest that the orientation fabric may evolve locally over a sticky spot to enhance ice for shear deformation to such an extent that the sticky spot may be difficult to infer by inverting for f using Glen's flow law (Fig. 7a1). Although not completely hidden, the peak-to-bottom value of f^2 is much reduced compared to the reference inversions based on Johnson's law. In practice, however, we speculate that real inversions for f in the presence of noisy input fields might make it difficult to discern whether a sticky spot exists at all using Glen's law. This is not to say that Johnson's law is a preferable choice for real inversions (let alone practical), or that other uncertainties are of less concern, such as temperature uncertainties or the limited obtainable resolution by self-adjoint methods in the presence of noise (Martin and Monnier, 2014), but rather that fabric might *additionally* obscure interpretations. The resulting basal drag over the asperity is, however, comparable to that inferred using Johnson's law (Fig. 7b1), although noise and the non-constant

background drag inferred using Glen's law might in practice also obscure interpretations.

In the case of the bed bump model (Fig. 7a2), inferring f using Glen's law results in a slippery spot at the bump peak where there is none (with a magnitude sensitive to the amount of regularisation chosen, as indicated by the lighter blue lines), and relative sticky flanks. The corresponding basal drag (Fig. 7b2) leads to the same conclusion.

Given these results, we conjecture that a sticky spot might generally cause the orientation fabric to evolve in such a way as to oppose the effect of the sticky spot, and that a bed bump might cause the orientation fabric to evolve in such a way as to make it incorrectly appear slippery on top and sticky on the flanks, thus dampening the effect of the bump. Indeed, when inferring the corresponding isotropic enhancement factor fields (Figs 8a, b), an isotropic softening is found in the aforementioned areas. Note that the inferred isotropic enhancements are locally >5, corresponding in magnitude to temperature anomalies of $\sim$5–10 $^\circ$C depending on activation energy.

Mass-flux estimates

The difference in background values of f^2 between the Johnson and Glen inversions are expected given the fabric field: from the point of view of the surface velocity field, a uniformly shear-
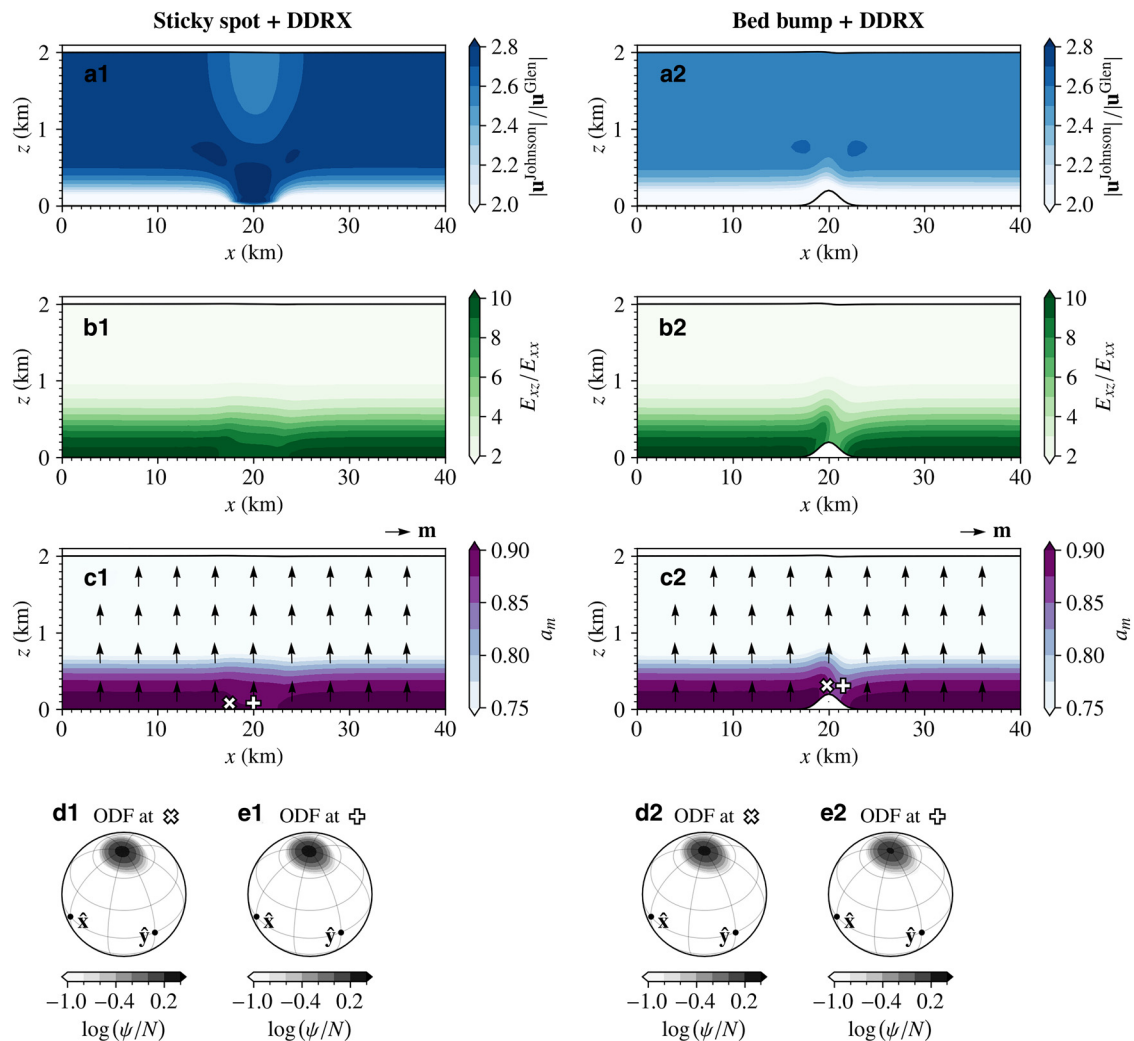
Fig. 6. Steady states of the sticky spot model (a1–e1) and the bed bump model (a2–e2) with DDRX. See Fig. 5 for shared descriptions.

enhanced layer (due to fabric) will have the same effect as uniformly decreasing f^2. If one is interested in inferring anomalies in f^2 compared to a background value (given the above caveat), this is possibly of little concern. On the contrary, care must be exercised when calculating vertically integrated mass fluxes because assuming Glen's law might lead to more sliding being inferred than is actually the case (too small f^2). The vertically integrated horizontal mass flux is by definition

$$\Phi(x) = \rho \int_{b(x)}^{s(x)} u_x(x, y) \mathrm{d}y. \tag{29}$$

If f is inferred with A given, Figs 7d1, d2 show that assuming isotropic ice (Glen's law) in our 2-D models leads to Φ being overestimated by ∼10% (compared to the true flux). If, on the other hand, E (or A) is inferred with f given, the corresponding mass-flux error is reduced to ∼2–3% (Fig. 8h). Note that the non-constant fluxes in the Glen-based inversions suggested non-zero emergence velocities (recall we constrain only the horizontal surface-velocity component). Although surface relaxation is often resorted to get rid of the incompatible kinematic free-surface boundary condition (e.g. Zhao and others, 2018), here it is sufficiently clear that the average fluxes are larger than the true fluxes.

Unless flow approximations are adopted for real ice masses that alleviate the mass-flux errors due to neglecting fabric, our results support jointly inferring f and A as a way to reduce mass-flux errors caused by missing fabric information, if inversion procedures can be constructed to overcome the increased underdeterminedness of joint inversions. Further research is needed to determine how exactly this affects mass-loss projections; while our results suggest that the present-day mass flux might be overestimated if only f is inferred (depending on flow approximation), the change in response to a climatic perturbation is not clear. Nor is it clear how these mass-flux errors translate to more realistic 3-D models where asperities are compactly defined, or to what extent it is possible to isotropically compensate for fabric in the popular vertically integrated 'block flow' or shallow shelf approximation (ideal limit of no internal deformation, a popular approximation for ice streams and fast-flowing outlet glaciers).

It is important to emphasise that the stress balance does not change by accounting for fabric anisotropy. Rather, the rate-of-deformation is (directionally) enhanced for given stress. In the block-flow approximation, vertical shear is taken to be negligible even when favoured by the orientation fabric. If, however, shear-enhanced layers due to fabric are in fact common, internal deformation may be more relevant in ice streams than isotropic models indicate, perhaps calling into question the assumption of block flow in some parts of ice streams. Observations of orientation fabrics in ice streams have found horizontal (or partially horizontal) girdle patterns, thought to be a signature of significant extensional flow (Smith and others, 2017) in agreement with Alley (1992). This should, in principle, harden the ice for further extension. Although our model setup
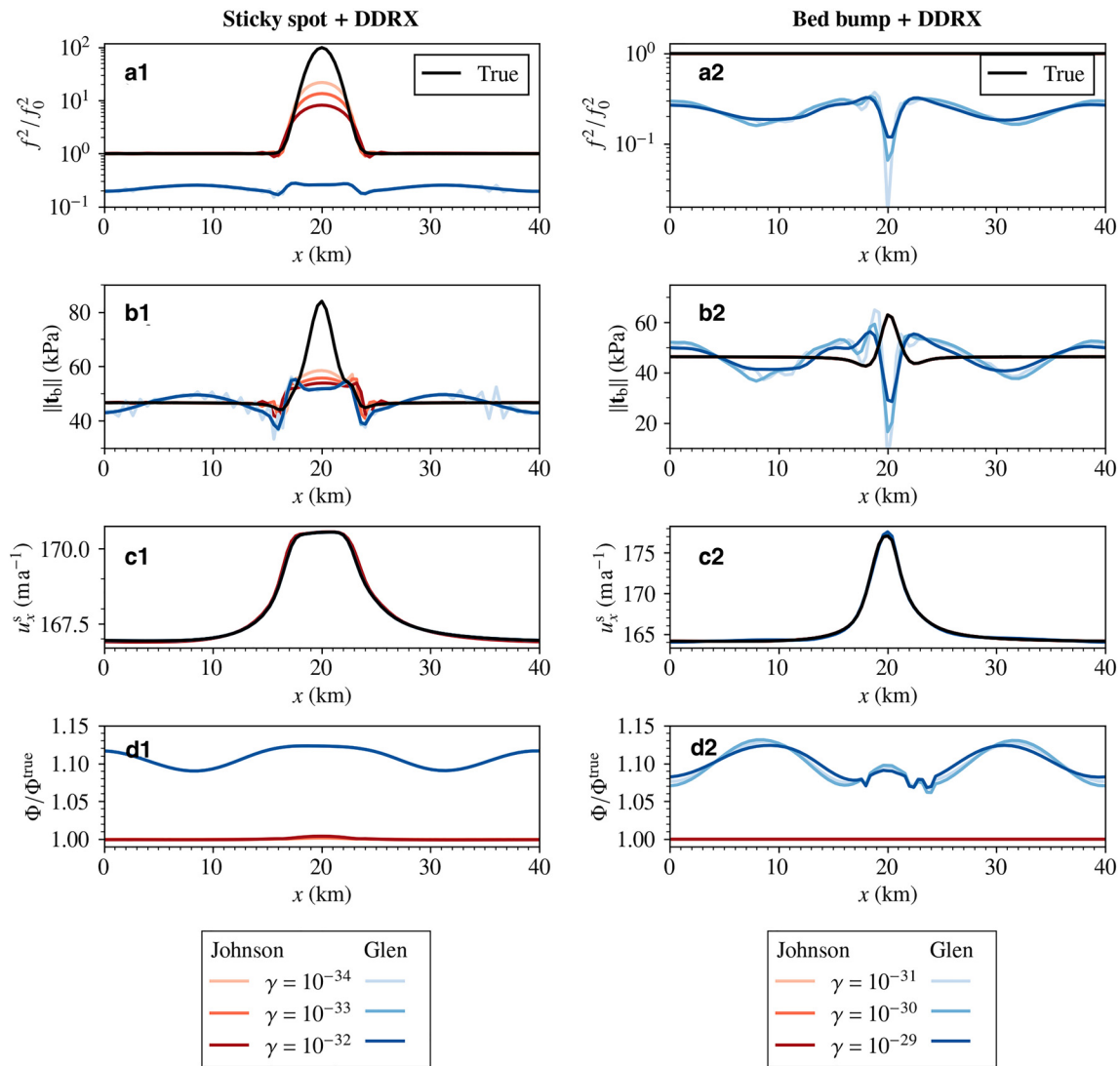
Fig. 7. Inverted sliding-law friction coefficients (a1 and a2), resulting basal drag (b1 and b2), resulting horizontal surface velocity component (c1 and c2), and resulting vertically integrated horizontal mass fluxes (d1 and d2). Left- and right-hand panels show the results for the sticky spot and bed bump model, respectively. Red and blue lines denote inversions using Johnson's and Glen's flow law, respectively, carried out for different strengths of regularisation (lighter/darker lines).

cannot produce that kind of extensional/compressional flow regime, it is (arguably) not settled to what extent ice streams and fast-flowing outlet glaciers can be approximated as ideal block flows throughout.

Caveats

At this point, several caveats are in order. For simplicity, a 2-D ice mass was considered, but it is not clear whether our results carry over to a more realistic 3-D model. It is possible that the identified effects are much more localised and less important in 3-D models. On the other hand, the 2-D scenarios considered here allow for the greatest chance of inferring the true basal friction field, since introducing greater complexity with a 3-D model should only make inferring f more difficult (not to mention A).

Related to the model realism, it is not clear how the DDRX rate factor, Γ_0, functionally depends on temperature, stress, strain rate, and dislocation density, although Richards and others (2021) has taken first steps to address this. Fabrics generally evolve differently in recrystallisation-dominated regimes compared to regimes where lattice rotation acts alone, not least if temperature is allowed to evolve (setting up a thermal–fabric feedback). However, as long

as vertical shear stresses are dominant, such as in our model simulations, the corresponding orientation decay rate (Fig. 3c) indicates that any strain-induced vertical single-maximum fabric should be reinforced by DDRX regardless of Γ_0. Put differently, unless compressional (extensional) stresses before (after) the sticky spot or bed bump are sufficiently large, the contribution to the decay rate from compressional (extensional) stress regimes (Fig. 3b) is subordinate. This could explain why our results are similar both with and without DDRX. Moreover, if vertical shear is dominant, this might partly explain why only minor fabric changes are found for non-linear sliding ($m = 3$). On that note, we also find similar steady-state fabric patterns upon multiplying the background friction coefficient, f_0^2, by a factor of 2 and 0.5, corresponding to steady-state sliding ratios of ~10 and 30% of the modelled surface speed.

We restricted ourselves to the case of a significant sticky spot (100 times the background value) and bed bump (10% of the ice thickness). For less strong perturbations, it is possible that inversions based on Glen's flow law give acceptable estimates of f (up to a constant). We mention that a higher bed slope (5°) and colder ice (-40 °C) were additionally considered, both leading to conclusions similar to those presented here. Likewise, similar steady-state
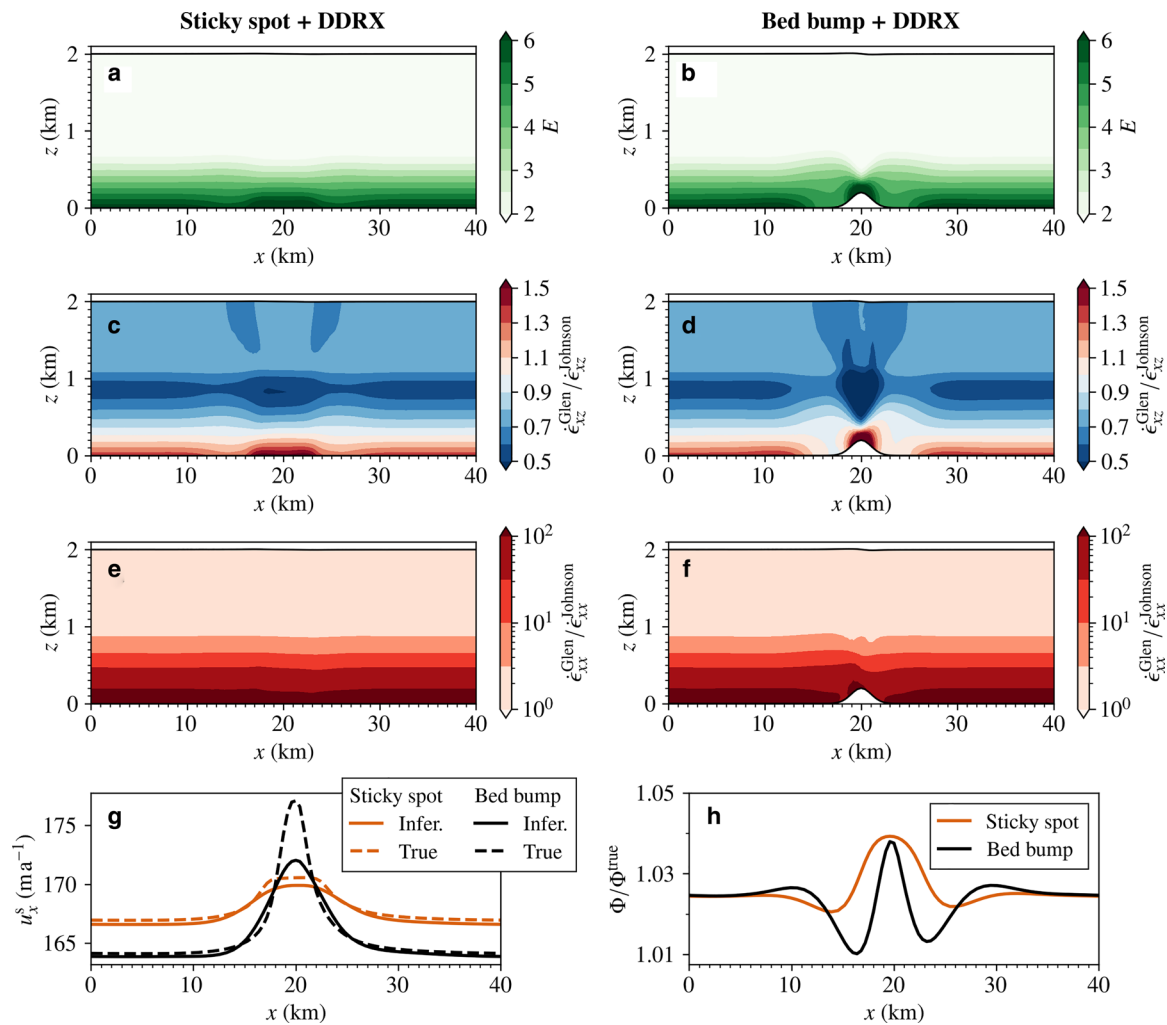
Fig. 8. Inferred equivalent isotropic enhancement factor, $E(x, y)$, for the sticky spot (a) and bed bump (b) model with DDRX. The shear and longitudinal strain rates resulting from Glen's law (E given) divided by those produced by Johnson's law (true fabric state given) are shown in panels c, d and e, f, respectively, for diagnostic shear and longitudinal stress states (see main text). Panel g shows the resulting horizontal surface velocity components (solid lines) compared to the true profiles (dashed lines). Panel h shows the corresponding vertically integrated mass flux profiles relative to the true profiles.

fabric patterns were also found upon increasing the Gaussian variance of the asperities by a factor of 2 and 4, corresponding to increasing the width of the asperities from ~2 to 3 and 5 ice thicknesses, respectively. The resulting inversions leave our conclusions unchanged, although fabric's effect on inversions is found to weaken with increasing wavelength of the basal asperities. Martin and Monnier (2014) considered adding 1% Gaussian noise to the horizontal surface velocities provided as input for an adjoint-based inversion, finding a lower bound of identifiable wavelengths in the friction coefficient on the order of several ice thicknesses. The fabric effect reported here might therefore be relevant over the length scales possible to infer in the presence of noise using adjoint-based inverse methods.

Given the bed slope and flow-rate factor (A) used in the presented simulations, the characteristic time taken for an ice parcel near the bed to pass over the asperities is ~50 a, depending on the state considered (transient or steady). This raises the question of whether the fabric of ice parcels, with trajectories over basal asperities, can in fact develop fast enough for our inversion results to be relevant for transient states of real ice masses, too. Our forward simulations without DDRX take ~50 a and 200 a before the orientation fabric develops enough to considerably affect inversions in the sticky spot and bed bump model, respectively. In a sense, this estimate represents an upper bound on the fabric adjustment timescale: the fabrics of real ice parcels approaching basal asperities are unlikely

to be isotropic, and hence the fabric adjustment time is likely less. If, however, DDRX is non-negligible, we underline that Γ_0 represents a separate characteristic timescale for DDRX. Indeed, given the right conditions, e.g. temperatures above $-10\,^{\circ}$C and near the bedrock, fabric evolution due to DDRX can be fast (Alley, 1992; De La Chapelle and others, 1998; Faria and others, 2014b). Although a more thorough investigation is needed, the modelled timescales characterising lattice rotation and DDRX suggests that our results are not necessarily restricted to steady state flows; that is, orientation fabrics might generally develop fast enough to affect inversions targeting transient states of real ice masses, too.

We leave the above caveats and questions for future research instead of exhausting a search through model space to determine the exact conditions under which fabric can have an effect. The point is here, rather, to demonstrate that it is possible for the orientation fabric to obscure the basal conditions and affect mass-flux estimates in addition to other rheological uncertainties.

Inferring basal conditions

In this study, we distinguished between a local increase in the friction coefficient and a bedrock bump, the former defined as a 'sticky spot'. The latter is sometimes also referred to as a sticky spot due to the resulting local increase in basal drag it can introduce (Alley, 1993; Stokes and others, 2007). Generally, there are

four possible mechanisms for locally increased drag (Stokes and others, 2007): (1) till-free areas, (2) areas of relatively strong till, (3) areas of freeze-on, and (4) bedrock bumps. In our parlance, the first three cases alter the friction coefficient field and are therefore indistinguishable from the point-of-view of the ice above, while the fourth (bed bump) is a distinctly different mechanism of increased drag. Given our results, the need for such a distinction is made clear; when using Glen's flow law, the inferred basal drag is much more accurate for a sticky spot than a bedrock bump (at least when inferring f in isolation). Because bedrock bumps can be small or simply located between sparse measurements, these two sources of 'effective' sticky spots can, however, not always be separated in practice. Both sources must therefore be considered when inferring basal conditions from inversions.

Unless jointly inferring f and A alleviates the problem, the distinct effect of sticky spots and bedrock bumps suggests that the accuracy of an inversion may vary within a single-drainage basin since roughness often changes along flow (Franke and others, 2021; Holschuh and others, 2020). Although our study focuses on flow regimes where both sliding and internal deformation are non-negligible (arguably relevant near ice-stream onsets), we end by noting that more research is needed to determine the relevance for flow regimes dominated by longitudinal and lateral (transverse) stresses, such as near fast-flowing outlet glaciers.

Conclusions

We investigated the isolated effect of neglecting the crystal-orientation fabric (mechanical anisotropies) when inferring the basal friction coefficient of a Weertman sliding law. Specifically, we considered two idealised cases of ice flowing over a sticky spot (increased friction coefficient) and a bedrock bump by using a vertical cross-section model, consisting of the anisotropic Johnson flow law, a mixed Taylor–Sachs grain rheology, and a spectral fabric model of lattice rotation and dynamic recrystallisation. Given the resulting anisotropic steady or transient states as input for an adjoint-based inversion procedure under the assumption of isotropic ice (Glen's flow law), we find that bedrock bumps can be misinterpreted as sticky on the flanks and slippery on top when in fact the slipperiness is uniform. When inferring the basal drag over a sticky spot, we find that assuming isotropic ice might be sufficient to identify the sticky spot, but in practice it may be obscured by regularisation and uncertainties in input fields, the latter known to limit the obtainable resolution of basal friction fields (Martin and Monnier, 2014). For both the sticky spot and bed bump models, fabric was allowed to evolve with and without discontinuous dynamic recrystallisation (nucleation and migration recrystallisation) near the bed. Due to the strong vertical shear regimes simulated, however, the resulting fabric patterns are close enough to produce similar results.

If instead the basal friction coefficient field is assumed to be known, we find that an isotropic enhancement factor field may be inferred to compensate for missing fabric information. Not only does this allow for surface velocities and vertically integrated mass fluxes be satisfactorily reproduced, but the resulting spatially distributed (isotropic) softening conforms with the softening suggested by the proper anisotropic enhancement factors and the flow speed ratios as modelled by Johnson's law compared to Glen's law. The price paid is, however, to render the material too soft when subject to longitudinal stresses. Our results therefore suggest that jointly inferring basal friction and the flow-rate factor in Glen's law might be a reasonable approach to reduce mass-flux errors by compensating for missing fabric information.

We emphasise that more research is needed to address the caveats raised (see 'Discussion'), and hence better determine the

physical conditions under which the identified fabric effect might exist. Specifically, our conclusions apply to 2-D flowline modelling where both sliding and internal deformation are non-negligible. The relevance for fast-sliding flow regimes (e.g. outlet systems) is not clear, and we cannot identify whether the equivalent isotropic enhancement factor could be depth-averaged for use in simple flow approximations. Nonetheless, the fact that the orientation fabric *can* hide (or at least obscure) the true basal boundary conditions from inversions suggests that care should be exercised when integrating mass fluxes under the assumption of isotropic ice, unless the flow-rate factor is jointly inferred or flow approximations otherwise alleviate the error caused by neglecting fabric. Similarly, care should be exercised when attempting relate subglacial conditions and processes to basal properties inferred from an inversion relying on Glen's flow law.

References

Advani SG and Tucker CL (1987) The use of tensors to describe and predict fiber orientation in short fiber composites. *Journal of Rheology* **31**(8), 751–784. doi: 10.1122/1.549945.

Alley RB (1988) Fabrics in polar ice sheets: development and prediction. *Science* **240**(4851), 493–495. doi: 10.1126/science.240.4851.493.

Alley RB (1992) Flow-law hypotheses for ice-sheet modeling. *Journal of Glaciology* **38**(129), 245–256. doi: 10.3189/S0022143000003658.

Alley RB (1993) In search of ice-stream sticky spots. *Journal of Glaciology* **39** (133), 447–454. doi: 10.3189/S0022143000016336.

Alley RB, Gow A and Meese D (1995) Mapping c-axis fabrics to study physical processes in ice. *Journal of Glaciology* **41**(137), 197–203. doi: 10.3189/S0022143000017895.

Alnæs MS, Logg A, Ølgaard KB, Rognes ME and Wells GN (2014) Unified form language: a domain-specific language for weak formulations of partial differential equations. *ACM Transactions on Mathematical Software* **40**(2), Article No. 9, 1–37. doi: 10.1145/2566630.

Anandakrishnan S and Alley RB (1997) Stagnation of Ice Stream C, West Antarctica by water piracy. *Geophysical Research Letters* **24**(3), 265–268. doi: 10.1029/96GL04016.

Arthern RJ (2015) Exploring the use of transformation group priors and the method of maximum relative entropy for Bayesian glaciological inversions. *Journal of Glaciology* **61**(229), 947–962. doi: 10.3189/2015JoG15J050.

Arthern RJ, Hindmarsh RCA and Williams CR (2015) Flow speed within the Antarctic ice sheet and its controls inferred from satellite observations. *Journal of Geophysical Research: Earth Surface* **120**(7), 1171–1188. doi: 10.1002/2014JF003239.

Azuma N (1995) A flow law for anisotropic polycrystalline ice under uniaxial compressive deformation. *Cold Regions Science and Technology* **23**(2), 137–147. doi: 10.1016/0165-232X(94)00011-L.

Azuma N and Higashi A (1985) Formation processes of ice fabric pattern in ice sheets. *Annals of Glaciology* **6**, 130–134. doi: 10.3189/1985AoG6-1-130-134.

Beyer S, Kleiner T, Aizinger V, Rückamp M and Humbert A (2018) A confined–unconfined aquifer model for subglacial hydrology and its application to the Northeast Greenland ice stream. *The Cryosphere* **12**(12), 3931–3947. doi: 10.5194/tc-12-3931-2018.

Brondex J, Gillet-Chaulet F and Gagliardini O (2019) Sensitivity of centennial mass loss projections of the Amundsen basin to the friction law. *The Cryosphere* **13**(1), 177–195. doi: 10.5194/tc-13-177-2019.

Castelnau O and Duval P (1994) Simulations of anisotropy and fabric development in polar ices. *Annals of Glaciology* **20**, 277–282. doi: 10.3189/1994AoG20-1-277-282.

Castelnau O, Duval P, Lebensohn RA and Canova GR (1996) Viscoplastic modeling of texture development in polycrystalline ice with a self-consistent approach: comparison with bound estimates. *Journal of Geophysical Research: Solid Earth* **101**(B6), 13851–13868. doi: 10.1029/96JB00412.

Christianson K and 7 others (2014) Dilatant till facilitates ice-stream flow in Northeast Greenland. *Earth and Planetary Science Letters* **401**, 57–69. doi: 10.1016/j.epsl.2014.05.060.

DeConto RM and Pollard D (2016) Contribution of Antarctica to past and future sea-level rise. *Nature* **531**(7596), 591–597. doi: 10.1038/nature17145.

De La Chapelle S, Castelnau O, Lipenkov V and Duval P (1998) Dynamic recrystallization and texture development in ice as revealed by the study of deep ice cores in Antarctica and Greenland. *Journal of Geophysical Research: Solid Earth* **103**(B3), 5091–5105. doi: 10.1029/97JB02621.

Durand G and 8 others (2007) Change in ice rheology during climate variations – implications for ice flow modelling and dating of the Epica Dome C core. *Climate of the Past* **3**(1), 155–167. doi: 10.5194/cp-3-155-2007.

Duval P, Ashby MF and Anderman I (1983) Rate-controlling processes in the creep of polycrystalline ice. *The Journal of Physical Chemistry* **87**(21), 4066–4074. doi: 10.1021/j100244a014.

Duval P and Castelnau O (1995) Dynamic recrystallization of ice in polar ice sheets. *Le Journal de Physique IV* **5**(C3), C3–C197. doi: 10.1051/jp4:1995317.

Echelmeyer KA, Harrison WD, Larsen C and Mitchell JE (1994) The role of the margins in the dynamics of an active ice stream. *Journal of Glaciology* **40**(136), 527–538. doi: 10.3189/S0022143000012417.

Fahnestock M, Abdalati W, Joughin I, Brozena J and Gogineni P (2001) High geothermal heat flow, basal melt, and the origin of rapid ice flow in Central Greenland. *Science* **294**(5550), 2338–2342. doi: 10.1126/science.1065370.

Faria SH, Weikusat I and Azuma N (2014a) The microstructure of polar ice. Part I: highlights from ice core research. *Journal of Structural Geology* **61**, 2–20. doi: 10.1016/j.jsg.2013.09.010.

Faria SH, Weikusat I and Azuma N (2014b) The microstructure of polar ice. Part II: state of the art. *Journal of Structural Geology* **61**, 21–49. doi: 10.1016/j.jsg.2013.11.003.

Franke S and 6 others (2021) Complex basal conditions and their influence on ice flow at the onset of the Northeast Greenland Ice Stream. *Journal of Geophysical Research: Earth Surface*, **n/a**(n/a), e2020JF005689. doi: 10.1029/2020JF005689.

Gagliardini O and 14 others (2013) Capabilities and performance of Elmer/Ice, a new-generation ice sheet model. *Geoscientific Model Development* **6**(4), 1299–1318. doi: 10.5194/gmd-6-1299-2013.

Gillet-Chaulet F and 8 others (2012) Greenland ice sheet contribution to sea-level rise from a new-generation ice-sheet model. *The Cryosphere* **6**(6), 1561–1576. doi: 10.5194/tc-6-1561-2012.

Gillet-Chaulet F, Gagliardini O, Meyssonnier J, Montagnat M and Castelnau O (2005) A user-friendly anisotropic flow law for ice-sheet modeling. *Journal of Glaciology* **51**(172), 3–14. doi: 10.3189/172756505781829584.

Gillet-Chaulet F, Gagliardini O, Meyssonnier J, Zwinger T and Ruokolainen J (2006) Flow-induced anisotropy in polar ice and related ice-sheet flow modelling. *Journal of Non-Newtonian Fluid Mechanics* **134**(1), 33–43. doi: 10.1016/j.jnnfm.2005.11.005.

Gödert G and Hutter K (1998) Induced anisotropy in large ice shields: theory and its homogenization. *Continuum Mechanics and Thermodynamics* **10**(5), 293–318. doi: 10.1007/s001610050095.

Greve R and Herzfeld UC (2013) Resolution of ice streams and outlet glaciers in large-scale simulations of the Greenland ice sheet. *Annals of Glaciology* **54**(63), 209–220. doi: 10.3189/2013AoG63A085.

Gudmundsson GH, Krug J, Durand G, Favier L and Gagliardini O (2012) The stability of grounding lines on retrograde slopes. *The Cryosphere* **6**(6), 1497–1505. doi: 10.5194/tc-6-1497-2012.

Hermann E and Barclay K (1998) Basal sliding of Ice Stream B, west Antarctica. *Journal of Glaciology* **44**(147), 223–230. doi: 10.3189/S0022143000002562.

Holschuh N, Christianson K, Paden J, Alley R and Anandakrishnan S (2020) Linking postglacial landscapes to glacier dynamics using swath radar at Thwaites Glacier, Antarctica. *Geology* **48**(3), 268–272. doi: 10.1130/G46772.1.

Hruby K and 5 others (2020) The impact of temperature and crystal orientation fabric on the dynamics of mountain glaciers and ice streams. *Journal of Glaciology* **66**(259), 755–765. doi: 10.1017/jog.2020.44.

Isaac T, Petra N, Stadler G and Ghattas O (2015) Scalable and efficient algorithms for the propagation of uncertainty from data through inference to prediction for large-scale problems, with application to flow of the Antarctic ice sheet. *Journal of Computational Physics* **296**, 348–368. doi: 10.1016/j.jcp.2015.04.047.

Johnson A (1977) Creep characterization of transversely-isotropic metallic materials. *Journal of the Mechanics and Physics of Solids* **25**(2), 117–126. doi: 10.1016/0022-5096(77)90007-2.

Joughin I, MacAyeal DR and Tulaczyk S (2004) Basal shear stress of the Ross ice streams from control method inversions. *Journal of Geophysical Research: Solid Earth* **109**(B9). doi: 10.1029/2003JB002960.

Joughin I, Smith BE and Howat IM (2018) A complete map of Greenland ice velocity derived from satellite data collected over 20 years. *Journal of Glaciology* **64**(243), 1–11. doi: 10.1017/jog.2017.73.

Joughin I, Smith BE and Schoof CG (2019) Regularized coulomb friction laws for ice sheet sliding: application to pine island glacier, Antarctica. *Geophysical Research Letters* **46**(9), 4764–4771. doi: 10.1029/2019GL082526.

Kamb WB (1961) The glide direction in ice. *Journal of Glaciology* **3**(30), 1097–1106. doi: 10.3189/S0022143000017500.

Kamb B (1972) Experimental recrystallization of ice under stress. *Washington DC American Geophysical Union Geophysical Monograph Series* **16**, 211–241.

Kamb B (2001) *Basal Zone of the West Antarctic Ice Streams and its Role in Lubrication of Their Rapid Motion*, 157–199. American Geophysical Union (AGU). doi: 10.1029/AR077p0157.

Keisling BA and 8 others (2014) Basal conditions and ice dynamics inferred from radar-derived internal stratigraphy of the Northeast Greenland Ice Stream. *Annals of Glaciology* **55**(67), 127–137. doi: 10.3189/2014AoG67A090.

Larour E, Seroussi H, Morlighem M and Rignot E (2012) Continental scale, high order, high spatial resolution, ice sheet modeling using the ice sheet system model (ISSM). *Journal of Geophysical Research: Earth Surface* **117**(F1). doi: 10.1029/2011JF002140.

Logg A, Mardal KA, Wells GN, and others (2012) *Automated Solution of Differential Equations by the Finite Element Method*. Springer. doi: 10.1007/978-3-642-23099-8.

MacAyeal DR (1993) A tutorial on the use of control methods in ice-sheet modeling. *Journal of Glaciology* **39**(131), 91–98. doi: 10.3189/S0022143000015744.

MacAyeal DR, Bindschadler RA and Scambos TA (1995) Basal friction of Ice Stream E, West Antarctica. *Journal of Glaciology* **41**(138), 247–262. doi: 10.3189/S0022143000016154.

Maier N, Gimbert F, Gillet-Chaulet F and Gilbert A (2021) Basal traction mainly dictated by hard-bed physics over grounded regions of Greenland. *The Cryosphere* **15**(3), 1435–1451. doi: 10.5194/tc-15-1435-2021.

Martin N and Monnier J (2014) Adjoint accuracy for the full stokes ice flow model: limits to the transmission of basal friction variability to the surface. *The Cryosphere* **8**(2), 721–741. doi: 10.5194/tc-8-721-2014.

Martín C and Gudmundsson GH (2012) Effects of nonlinear rheology, temperature and anisotropy on the relationship between age and depth at ice divides. *The Cryosphere* **6**(5), 1221–1229. doi: 10.5194/tc-6-1221-2012.

Martín C, Gudmundsson GH, Pritchard HD and Gagliardini O (2009) On the effects of anisotropic rheology on ice flow, internal structure, and the age-depth relationship at ice divides. *Journal of Geophysical Research: Earth Surface* **114**(F4). doi: 10.1029/2008JF001204.

Meyssonnier J and Philip A (1996) A model for the tangent viscous behaviour of anisotropic polar ice. *Annals of Glaciology* **23**, 253–261. doi: 10.3189/S0260305500013513.

Mitusch SK, Funke SW and Dokken JS (2019) dolfin-adjoint 2018.1: automated adjoints for FEniCS and Firedrake. *Journal of Open Source Software* **4**(38), 1292. doi: 10.21105/joss.01292.

Morlighem M, Seroussi H, Larour E and Rignot E (2013) Inversion of basal friction in Antarctica using exact and incomplete adjoints of a higher-order model. *Journal of Geophysical Research: Earth Surface* **118**(3), 1746–1753. doi: 10.1002/jgrf.20125.

Pettit EC, Thorsteinsson T, Jacobson HP and Waddington ED (2007) The role of crystal fabric in flow near an ice divide. *Journal of Glaciology* **53** (181), 277–288. doi: 10.3189/172756507782202766.

Pimienta P, Duval P and Lipenkov VY (1987) Mechanical behaviour of anisotropic polar ice. In *The Physical Basis of Ice Sheet Modelling*, IAHS Publication No. 170, 57–66, IAHS Press, Wallingford, UK.

Placidi L, Greve R, Seddik H and Faria SH (2010) Continuum-mechanical, anisotropic flow model for polar ice masses, based on an anisotropic flow enhancement factor. *Continuum Mechanics and Thermodynamics* **22**(3), 221–237. doi: 10.1007/s00161-009-0126-0.

Ranganathan M, Minchew B, Meyer CR and Gudmundsson GH (2020) A new approach to inferring basal drag and ice rheology in ice streams, with applications to West Antarctic Ice Streams. *Journal of Glaciology* **67** (262), 229–242. doi: 10.1017/jog.2020.95.

Rathmann NM, Hvidberg CS, Grinsted A, Lilien DA and Dahl-Jensen D (2021) Effect of an orientation-dependent non-linear grain fluidity on bulk directional enhancement factors. *Journal of Glaciology* **67**(263), 569–575. doi: 10.1017/jog.2020.117.

Richards DH, Pegler SS, Piazolo S and Harlen OG (2021) The evolution of ice fabrics: a continuum modelling approach validated against laboratory experiments. *Earth and Planetary Science Letters* **556**, 116718. doi: 10.1016/j.epsl.2020.116718.

Rückamp M, Greve R and Humbert A (2019) Comparative simulations of the evolution of the Greenland ice sheet under simplified Paris Agreement scenarios with the models SICOPOLIS and ISSM. *Polar Science*, **21**, 14–25. doi: 10.1016/j.polar.2018.12.003, iSAR-5/ Fifth International Symposium on Arctic Research.

Schoof C and Mantelli E (2021) The role of sliding in ice stream formation. *Proceedings of the Royal Society A: Mathematical, Physical and Engineering Sciences* **477**(2248), 20200870. doi: 10.1098/rspa.2020.0870.

Sergienko OV, Creyts TT and Hindmarsh RCA (2014) Similarity of organized patterns in driving and basal stresses of Antarctic and Greenland ice sheets beneath extensive areas of basal sliding. *Geophysical Research Letters* **41**(11), 3925–3932. doi: 10.1002/2014GL059976.

Shoji H and Langway CC (1985) *Mechanical Properties of Fresh Ice Core from Dye 3, Greenland*, 39–48. American Geophysical Union (AGU). doi: 10.1029/GM033p0039).

Shoji H and Langway CC (1988) Flow-law parameters of the dye 3, Greenland, deep ice core. *Annals of Glaciology* **10**, 146–150. doi: 10.3189/S026030550000433X.

Smith-Johnsen S, de Fleurian B, Schlegel N, Seroussi H and Nisancioglu K (2020) Exceptionally high heat flux needed to sustain the Northeast Greenland Ice Stream. *The Cryosphere* **14**(3), 841–854. doi: 10.5194/tc-14-841-2020.

Smith EC and 6 others (2017) Ice fabric in an Antarctic ice stream interpreted from seismic anisotropy. *Geophysical Research Letters* **44**(8), 3710–3718. doi: 10.1002/2016GL072093.

Staroszczyk R and Gagliardini O (1999) Two orthotropic models for strain-induced anisotropy of polar ice. *Journal of Glaciology* **45**(151), 485–494. doi: 10.3189/S0022143000001349.

Stokes CR, Clark CD, Lian OB and Tulaczyk S (2007) Ice stream sticky spots: a review of their identification and influence beneath contemporary and palaeo-ice streams. *Earth-Science Reviews* **81**(3), 217–249. doi: 10.1016/j.earscirev.2007.01.002.

Svendsen B and Hutter K (1996) A continuum approach for modelling induced anisotropy in glaciers and ice sheets. *Annals of Glaciology* **23**, 262–269. doi: 10.3189/S0260305500013525.

Thorsteinsson T (2001) An analytical approach to deformation of anisotropic ice-crystal aggregates. *Journal of Glaciology* **47**(158), 507–516. doi: 10.3189/172756501781832124.

Thorsteinsson T, Kipfstuhl J and Miller H (1997) Textures and fabrics in the grip ice core. *Journal of Geophysical Research: Oceans* **102**(C12), 26583–26599. doi: 10.1029/97JC00161.

Thorsteinsson T, Waddington ED and Fletcher RC (2003) Spatial and temporal scales of anisotropic effects in ice-sheet flow. *Annals of Glaciology* **37**, 40–48. doi: 10.3189/172756403781815429.

Tulaczyk S, Kamb WB and Engelhardt HF (2000) Basal mechanics of Ice Stream B, west Antarctica: 1. Till mechanics. *Journal of Geophysical Research: Solid Earth* **105**(B1), 463–481. doi: 10.1029/1999JB900329.

van der Veen C and Whillans I (1994) Development of fabric in ice. *Cold Regions Science and Technology* **22**(2), 171–195. doi: 10.1016/0165-232X(94)90027-2.

Weertman J (1957) On the sliding of glaciers. *Journal of Glaciology* **3**(21), 33–38. doi: 10.3189/S0022143000024709.

Weertman J (1973) Creep of ice. In *Physics and Chemistry of Ice*, 320–337, Royal Society of Canada, Ottawa, Canada.

Whillans IM, van der Veen CJ (1997) The role of lateral drag in the dynamics of Ice Stream B, Antarctica. *Journal of Glaciology* **43**(144), 231–237. doi: 10.3189/S0022143000003178.

Zhao C and 5 others (2018) Basal friction of Fleming Glacier, Antarctica – part 1: sensitivity of inversion to temperature and bedrock uncertainty. *The Cryosphere* **12**(8), 2637–2652. doi: 10.5194/tc-12-2637-2018.

Zoet LK and Iverson NR (2020) A slip law for glaciers on deformable beds. *Science* **368**(6486), 76–78. doi: 10.1126/science.aaz1183.

Appendix A. Taylor enhancement factor

The Taylor-averaged linear Johnson grain rheology is given by (Rathmann and others, 2021)

$$
\begin{aligned}
\langle \boldsymbol{\tau}' \rangle = A' \Bigg(& \dot{\boldsymbol{\epsilon}} - \frac{E_{cc}'^{-1} - 1}{2} (\dot{\boldsymbol{\epsilon}} \cdot\cdot \langle \mathbf{c}^2 \rangle)\mathbf{I} \\
& + \frac{3(E_{cc}'^{-1} - 1) - 4(E_{ca}'^{-1} - 1)}{2} \dot{\boldsymbol{\epsilon}} \cdot\cdot \langle \mathbf{c}^4 \rangle \\
& + (E_{ca}'^{-1} - 1)(\dot{\boldsymbol{\epsilon}} \cdot \langle \mathbf{c}^2 \rangle + \langle \mathbf{c}^2 \rangle \cdot \dot{\boldsymbol{\epsilon}}) \Bigg).
\end{aligned}
\tag{A1}
$$

Vectorising $\langle \boldsymbol{\tau}' \rangle$ and $\dot{\boldsymbol{\epsilon}}$ according to

$$
\mathcal{V}(X_{ij}) = \left[X_{11}, X_{21}, X_{31}, X_{12}, \ldots, X_{33} \right]^T,
$$

Eqn (A1) may be written as the 9×9 linear problem

$$
\mathbf{P} \cdot \mathcal{V}(\dot{\boldsymbol{\epsilon}}) = \mathcal{V}(\langle \boldsymbol{\tau}' \rangle),
\tag{A2}
$$

where

$$
\begin{aligned}
\mathbf{P} = \mathbf{I}_9 & - \frac{E_{cc}'^{-1} - 1}{2} \mathbf{I} \otimes \langle \mathbf{c}^2 \rangle \\
& + \frac{3(E_{cc}'^{-1} - 1) - 4(E_{ca}'^{-1} - 1)}{2} \mathcal{F}(\langle \mathbf{c}^4 \rangle) \\
& + (E_{ca}'^{-1} - 1)(\mathbf{I} \otimes \langle \mathbf{c}^2 \rangle + \langle \mathbf{c}^2 \rangle \otimes \mathbf{I})
\end{aligned}
\tag{A3}
$$

is a 9×9 matrix that depends on the second- and forth-order structure tensors, $\otimes$ is the generalised outer product (Kronecker product), and

$$
\mathcal{F}(X_{ijlm}) = \begin{bmatrix}
X_{1111} & X_{1121} & X_{1131} & X_{1112} & \cdots & X_{1133} \\
X_{2111} & X_{2121} & X_{2131} & X_{2112} & \cdots & X_{2133} \\
\vdots & \vdots & \vdots & \vdots & & \vdots \\
X_{3311} & X_{3321} & X_{3331} & X_{3312} & \cdots & X_{3333}
\end{bmatrix}.
$$

The forward form of the Taylor-averaged grain rheology (A2) is therefore

$$
\dot{\boldsymbol{\epsilon}}(\langle \boldsymbol{\tau}' \rangle) = \mathcal{V}^{-1}\left(\mathbf{P}^{-1} \cdot \mathcal{V}(\langle \boldsymbol{\tau}' \rangle) \right),
\tag{A4}
$$

where $\mathcal{V}^{-1}$ reverts the vectorisation.

Note that for small and large values of E_{cc}' and E_{ca}', respectively, Eqn (A2) may be ill-conditioned. In that case, solving the Tikhonov regularised problem

$$
\left(\mathbf{P}^T \cdot \mathbf{P} + \lambda \mathbf{I}_9 \right) \cdot \mathcal{V}(\dot{\boldsymbol{\epsilon}}) = \mathbf{P}^T \cdot \mathcal{V}(\langle \boldsymbol{\tau}' \rangle),
\tag{A5}
$$

was found to provide good estimates of $\mathcal{V}(\dot{\boldsymbol{\epsilon}})$ for $\lambda = 10^{-6}$.

Appendix B. Dynamic recrystallisation

In order to calculate the time-evolution of the fabric expansion coefficients due to DDRX, it is helpful to adopt the bra-ket notation for characterising the fabric state:

$$|\psi(\mathbf{x}, t, \theta, \phi)\rangle = \psi_l^m(\mathbf{x}, t)|Y_l^m(\theta, \phi)\rangle, \tag{B1}$$

where summation over repeated l and m is implied. Given Eqn (B1), the expansion coefficients, ψ_l^m, follow directly from calculating the overlap between Y_l^m and ψ:

$$\langle Y_l^m|\psi\rangle = \langle Y_l^m|Y_{l'}^{m'}\rangle\psi_{l'}^{m'} = \psi_l^m, \tag{B2}$$

where the overlap between any two arbitrary functions X and Y on S^2 is given by

$$\langle X|Y\rangle = \int_{S^2} X^* Y \mathrm{d}\Omega, \tag{B3}$$

and $\langle Y_l^m|Y_{l'}^{m'}\rangle = \delta_{l,l'}\delta_{m,m'}$ by definition since Y_l^m are mutually orthogonal. The Eulerian rate-of-change of the expansion coefficients,

$$\dot{\psi}_l^m = \langle Y_l^m|\dot{\psi}\rangle, \tag{B4}$$

due to recrystallisation is therefore

$$\dot{\psi}_l^m = \Gamma_0\langle Y_l^m|D|Y_{l'}^{m'}\rangle\psi_{l'}^{m'} - \Gamma_0\langle D\rangle\psi_l^m. \tag{B5}$$

If D is expanded in terms of Y_l^m, the matrix elements $\langle Y_l^m|D|Y_{l'}^{m'}\rangle$ in Eqn (B5) reduce to a linear combination of Gaunt coefficients (overlap integrals involving triple products in Y_l^m). Following Rathmann and others (2021), considerable notational simplicity may be achieved by writing $\boldsymbol{\tau}$ in terms of the expansion coefficients of the quadric surface $\boldsymbol{\tau} \cdots \mathbf{cc}$, defined as

$$\tau_l^m = \langle Y_l^m|\boldsymbol{\tau} \cdots \mathbf{cc}\rangle, \tag{B6}$$

which evaluate exactly to (i.e. higher wave-number coefficients vanish)

$$\tau_0^0 = \frac{2}{3}\sqrt{\pi}\,\mathrm{tr}(\boldsymbol{\tau}) \quad \tau_2^0 = -\frac{2}{3}\sqrt{\frac{\pi}{5}}(\tau_{xx} + \tau_{yy} - 2\tau_{zz}),$$

$$\tau_2^{-1} = 2\sqrt{\frac{2\pi}{15}}(\tau_{xz} + i\tau_{yz}) \quad \tau_2^1 = -(\tau_2^{-1})^*,$$

$$\tau_2^{-2} = \sqrt{\frac{2\pi}{15}}(\tau_{xx} - \tau_{yy} + 2i\tau_{xy}) \quad \tau_2^2 = (\tau_2^{-2})^*,$$

and $\boldsymbol{\tau}$ is therefore exactly

$$\boldsymbol{\tau} = \frac{1}{4}\sqrt{\frac{15}{2\pi}}\begin{bmatrix} \tau_2^{-2} + \tau_2^2 - \sqrt{\frac{2}{3}}\tau_2^0 & -i(\tau_2^{-2} - \tau_2^2) & \tau_2^{-1} - \tau_2^1 \\ & -\tau_2^{-2} - \tau_2^2 - \sqrt{\frac{2}{3}}\tau_2^0 & -i(\tau_2^{-1} + \tau_2^1) \\ \text{sym.} & & 2\sqrt{\frac{2}{3}}\tau_2^0 \end{bmatrix}. \tag{B7}$$

Expressing $\mathbf{c}^2$ and $\mathbf{c}^4$ in terms of Y_l^m, D can be written as (verified in Mathematica)

$$D = \frac{3}{28}\sqrt{\frac{5}{\pi}}(g_0 Y_0^0 + \mathbf{g}_2 \cdot \mathbf{Y}_2 + \mathbf{g}_4 \cdot \mathbf{Y}_4), \tag{B8}$$

where

$$\mathbf{Y}_2 = [Y_2^{-2}, Y_2^{-1}, Y_2^0, Y_2^1, Y_2^2]^T, \tag{B9}$$

$$\mathbf{Y}_4 = [Y_4^{-4}, Y_4^{-3}, Y_4^{-2}, Y_4^{-1}, Y_4^0, Y_4^1, Y_4^2, Y_4^3, Y_4^4]^T, \tag{B10}$$

and the stress-dependent coupling weights are

$$g_0(\boldsymbol{\tau}) = \frac{7}{\sqrt{5}}\left((\tau_2^0)^2 - 2\tau_2^{-1}\tau_2^1 + 2\tau_2^{-2}\tau_2^2\right), \tag{B11}$$

$$\mathbf{g}_2(\boldsymbol{\tau}) = \begin{bmatrix} \sqrt{3/2}(\tau_2^{-1})^2 - 2\tau_2^0\tau_2^{-2} \\ \tau_2^0\tau_2^{-1} - \sqrt{6}\tau_2^1\tau_2^{-2} \\ (\tau_2^0)^2 - \tau_2^{-1}\tau_2^1 - 2\tau_2^{-2}\tau_2^2 \\ \tau_2^0\tau_2^1 - \sqrt{6}\tau_2^{-1}\tau_2^2 \\ \sqrt{3/2}(\tau_2^1)^2 - 2\tau_2^0\tau_2^2 \end{bmatrix}, \tag{B12}$$

$$\mathbf{g}_4(\boldsymbol{\tau}) = \frac{-4}{3}\begin{bmatrix} \sqrt{14}/2(\tau_2^{-2})^2 \\ \sqrt{7}\tau_2^{-1}\tau_2^{-2} \\ \sqrt{2}(\tau_2^{-1})^2 + \sqrt{3}\tau_2^0\tau_2^{-2} \\ \sqrt{6}\tau_2^0\tau_2^{-1} + \tau_2^1\tau_2^{-2} \\ \sqrt{1/5}(3(\tau_2^0)^2 + 4\tau_2^{-1}\tau_2^1 + \tau_2^{-2}\tau_2^2) \\ \sqrt{6}\tau_2^0\tau_2^1 + \tau_2^{-1}\tau_2^2 \\ \sqrt{2}(\tau_2^1)^2 + \sqrt{3}\tau_2^0\tau_2^2 \\ \sqrt{7}\tau_2^1\tau_2^2 \\ \sqrt{14}/2(\tau_2^2)^2 \end{bmatrix}. \tag{B13}$$

Although $\langle D\rangle$ can be calculated directly from the definition

$$\langle D\rangle = \frac{(\boldsymbol{\tau} \cdot \boldsymbol{\tau}) \cdots \langle \mathbf{c}^2\rangle - \boldsymbol{\tau} \cdots \langle \mathbf{c}^4\rangle \cdots \boldsymbol{\tau}}{\boldsymbol{\tau} \cdots \boldsymbol{\tau}}, \tag{B14}$$

given the second- and fourth-order structure tensors, we note that the conservation constraint

$$0 = \dot{N} = \int_{S^2} \dot{\psi}\mathrm{d}\Omega = \sqrt{4\pi}\dot{\psi}_0^0 \tag{B15}$$

implies that $\langle D\rangle$ is, by virtue of Eqn (B5), nothing but the inner product

$$\langle D\rangle = \frac{\langle Y_0^0|D|Y_{l'}^{m'}\rangle\psi_{l'}^{m'}}{\psi_0^0}. \tag{B16}$$

Hence, the term containing $\langle D\rangle$ in Eqn (B5) is nonlinear.

In summary, the effect of recrystallisation is represented by a linear transformation of ψ_l^m and a common nonlinear scaling transformation of ψ_l^m (for all l and m), both depending on $\boldsymbol{\tau}$.

Appendix C. Weak forms

Stokes problem

Forming the inner product between the stress balance, $-\nabla \cdot \boldsymbol{\tau} + \nabla p = \rho\mathbf{g}$, and a vector weight function $\mathbf{v}$, and adding the incompressibility condition, $\nabla \cdot \mathbf{u} = 0$, multiplied by the weight function q, the weak Stokes problem follows from integrating the result over the model domain:

$$\int [\boldsymbol{\tau} \cdots \nabla\mathbf{v} + q\nabla \cdot \mathbf{u} - p\nabla \cdot \mathbf{v}]\mathrm{d}\mathbf{x} - \int_{\Gamma_b} \mathbf{v} \cdot \mathbf{t}_b \mathrm{d}l$$
$$+ \int_{\Gamma_b} [w\mathbf{u} \cdot \hat{\mathbf{n}} - \lambda\mathbf{v} \cdot \hat{\mathbf{n}}]\mathrm{d}l = \int \rho\mathbf{g} \cdot \mathbf{v}\mathrm{d}\mathbf{x}, \tag{C1}$$

where second-order derivatives were integrated by parts, the surface Γ_s is assumed stress free ($\boldsymbol{\sigma} \cdot \hat{\mathbf{n}} = \mathbf{0}$), $\rho = 917$ kg m^{-3} is the density of ice, $\mathbf{g}$ is the gravitational acceleration, $\mathbf{t}_b$ is the basal traction given by the sliding law, and $\boldsymbol{\tau}(\dot{\boldsymbol{\epsilon}})$ is the flow law. The mixed variational problem (C1) was discretised using Taylor–Hood elements for both the unknowns and weight functions (Galerkin method), i.e. linear elements for p and q, and quadratic elements for $\mathbf{u}$ and $\mathbf{v}$. The term additionally added to Eqn (C1) weakly imposes $\mathbf{u} \cdot \hat{\mathbf{n}} = 0$ on Γ_b through a Lagrange multiplier field, λ, and its weight function,

w (both linear elements). Note that the Cauchy stress-vector component normal to the basal boundary is absorbed into λ.

Free-surface evolution

The free-surface equation was discretised in time using a backward Euler scheme. Upon multiplying by a weight function, w, and integration over the domain length, its weak form is given by

$$\frac{1}{\Delta t}\int [s(t_{k+1}) - s(t_k)]w\,dx = \int \left[u_z^s - u_x^s \frac{ds(t_{k+1})}{dx}\right] w\,dx \\ - \nu_s \int \frac{ds(t_{k+1})}{dx}\frac{dw}{dx}\,dx, \tag{C2}$$

where k is the time-step index. The term additionally added to the right-hand is a Laplacian term (having been integrated by parts) for numerical stability. The weak form (C2) was discretised in space using linear elements for both s and w (Galerkin method), and $\nu_s = 1 \times 10^{-3}$ m^2 s^{-1} was found to suffice.

Fabric evolution

Adding the models for lattice rotation and recrystallisation from the main text, the number distribution evolves according to

$$\dot\psi + (\mathbf{u}\cdot\nabla)\psi + \nabla_{S^2}\cdot(\psi\dot{\mathbf{c}}) = \Gamma\psi + \nu_\psi^\dagger \nabla_{S^2}^2\psi + \nu_\psi\nabla^2\psi. \tag{C3}$$

The two terms additionally added to the right-hand side provide Laplacian regularisation in orientation space and real space depending on the diffusion coefficients $\nu_\psi^\dagger$ and ν_ψ, respectively; the former required for any spectral truncation of ψ (Rathmann and others, 2021), the latter needed to stabilise fabric evolution for the finite-element discretisation used (more sophisticated stabilisation techniques were not attempted).

Calculating the rate-of-change of ψ_l^m using Eqn (B4) with (C3), it follows that

$$\dot\psi_l^m + (\mathbf{u}\cdot\nabla)\psi_l^m + \langle Y_l^m|R|Y_{l'}^{m'}\rangle\psi_{l'}^{m'} = \Gamma_0(\langle Y_l^m|D|Y_{l'}^{m'}\rangle\psi_{l'}^{m'} - \langle D\rangle\psi_l^m) \\ - \nu_\psi^\dagger l(l+1)\psi_l^m + \nu_\psi\nabla^2\psi_l^m, \tag{C4}$$

where $R = R(\dot{\boldsymbol\epsilon}, \boldsymbol\omega)$ is a linear operator representing the effect of c-axis rotation (see Rathmann and others (2021) for details), and the identity $\nabla^2 Y_l^m = -l(l+1)Y_l^m$ was used.

Equation (C4) implies a nonlinear system must be solved per computational node in order to evolve the fabric field (a 66-dimensional system in the case of $L = 10$ used in this study). In our numerical implementation, however, we linearised the problem by using a backward Euler time-discretisation scheme for all terms but $\langle D\rangle$. Upon multiplying by a weight function, ζ, and integration over the model domain, the corresponding weak form of (C4) is given by

$$\frac{1}{\Delta t}\int \left[\psi_l^m(t_{k+1}) - \psi_l^m(t_k)\right]\zeta\,d\mathbf{x} + \int \left[(\mathbf{u}\cdot\nabla)\psi_l^m(t_{k+1})\right]\zeta\,d\mathbf{x} \\ + \int \langle Y_l^m|R|Y_{l'}^{m'}\rangle\psi_{l'}^{m'}(t_{k+1})\zeta\,d\mathbf{x} \\ = \int \Gamma_0 \left[\langle Y_l^m|D|Y_{l'}^{m'}\rangle\psi_{l'}^{m'}(t_{k+1}) - \left(\frac{\langle Y_0^0|D|Y_{l'}^{m'}\rangle\psi_{l'}^{m'}(t_k)}{\psi_0^0(t_k)}\right)\psi_l^m(t_{k+1})\right]\zeta\,d\mathbf{x} \\ - \nu_\psi^\dagger l(l+1)\int \psi_l^m(t_{k+1})\zeta\,d\mathbf{x} - \nu_\psi\int \nabla\psi_l^m(t_{k+1})\cdot\nabla\zeta\,d\mathbf{x}, \tag{C5}$$

where k is the time-step index, and the last term in (C4) was integrated by parts assuming $\nabla\psi\cdot\hat{\mathbf{n}} = 0$ on the bedrock boundary. The form (C5) was discretised in space using linear elements for both ψ_l^m and ζ (Galerkin method).

We end by noting that in all forward simulations presented here, hyper diffusion on S^2 was used by setting $l(l+1) \to [l(l+1)]^2$, thereby further reducing the influence that regularisation has on the lowest wavenumber modes ($l \leq 4$) which E_{mm} and E_{mt} depend on. With this choice, regularisation is $[10(10+1)/4(4+1)]^2 \simeq 30$ times stronger for modes with $l = 10$ compared to $l = 4$. In all forward simulations, regularisation corresponding to $\nu_\psi = 5 \times 10^{-5}$ and $\nu_\psi^\dagger = 1 \times 10^{-4} \|\dot{\boldsymbol\epsilon}\|$ was used, the strain rate dependence of the latter following the fabric model of the numerical ice-flow model Elmer Ice (Gillet-Chaulet and others, 2005).